Journal of Materials Chemistry A

ROYAL SOCIETY OF CHEMISTRY

REVIEW

View Article Online
View Journal | View Issue

Cite this: J. Mater. Chem. A, 2025, 13, 33080

Emerging innovations in polymeric hollow fiber membranes for sustainable natural gas valorization

Xing Liu,[abc] Zhenyuan Li,[b] Zanchun Du,[b] Can Wang,[b] Haitao Zhang,[b] Shuangjiang Luo *[ab] and Suojiang Zhang *[b]

Polymeric hollow fiber membranes (HFMs) have emerged as a transformative technology for sustainable natural gas valorization, offering energy-efficient solutions for acid gas (CO_2 and H_2S) removal and helium (He) recovery. This review highlights recent advancements in material design, fabrication strategies, and performance optimization of HFMs tailored for aggressive natural gas feeds. Key innovations include the engineering of polymer structures, coupled with asymmetric architectures (dual-layer, thin-film composites), which overcome the intrinsic permeance-selectivity trade-off, achieving industrially relevant permeance and selectivities. Advanced mitigation strategies for membrane aging and plasticization, including crosslinking and siloxane hybridization, are elucidated at the molecular level, demonstrating enhanced stability under high-pressure conditions. Furthermore, breakthroughs in processing techniques (*e.g.*, co-extrusion spinning and interfacial polymerization) enable the fabrication of ultra-thin selective layers with defect-free interfaces. Emerging tools like machine learning and green solvents are also discussed as enablers of scalable and eco-friendly manufacturing. This work provides a comprehensive roadmap for next-generation HFMs, bridging molecular design with industrial deployment to advance decarbonization in energy systems. By addressing critical challenges and future opportunities, this review aims to inspire further research in high-performance membrane materials for sustainable natural gas processing.

Received 13th June 2025
Accepted 13th August 2025

DOI: 10.1039/d5ta04814a

rsc.li/materials-a

[a]Shanxi-Zheda Institute of Advanced Materials and Chemical Engineering, Taiyuan, 030000, China. E-mail: sjluo@ipe.ac.cn
[b]CAS Key Laboratory of Green Process and Engineering, Beijing Key Laboratory of Solid State Battery and Energy Storage Process, State Key Laboratory of Mesoscience and Engineering, Institute of Process Engineering, Chinese Academy of Sciences, Beijing 100190, China. E-mail: sjzhang@ipe.ac.cn
[c]University of Chinese Academy of Sciences, Beijing 101408, China

Xing Liu

Xing Liu is currently pursuing a PhD degree under the supervision of Prof. Shuangjiang Luo at the Institute of Process Engineering, Chinese Academy of Sciences. Her research focuses on microporous structure engineering and tailoring of hollow fiber membranes for noble gas separation.

Shuangjiang Luo

Shuangjiang Luo obtained his PhD from the Institute of Chemistry, Chinese Academy of Sciences in 2013. Following his post-doctoral experience at the University of Notre Dame and King Abdullah University of Science and Technology, he became a professor at the Institute of Process Engineering, Chinese Academy of Sciences in 2019. His main research interests include membrane-mediated gas separation, hollow fiber membranes, molecular recognition and adsorption, system integration and process design. He has published over 100 peer-reviewed articles and is a recipient of the IECR 2023 Class of Influential Researchers, RINENG Young Investigator Award, Beijing Nova Program of Science and Technology, etc.

1 Introduction

Natural gas has emerged as a critical pillar in the global energy transition, offering a pragmatic balance between escalating energy demands and decarbonization imperatives.[1] Its combustion emits 40–50% less CO_2 per unit energy than that of coal and oil, coupled with higher calorific efficiency and negligible particulate emissions, positioning it as a transitional fuel toward net-zero goals.[2] Global consumption has surged from 14.56% of primary energy in 1965 to 23.30% today, with a projected 12% growth by 2030.[3] However, raw natural gas is rarely pristine, containing corrosive impurities such as carbon dioxide (CO_2) and hydrogen sulfide (H_2S), which necessitate purification to meet pipeline specifications (<2% CO_2, <4 ppm H_2S) and mitigate infrastructure corrosion.[4,5] Concurrently, select reservoirs harbor helium (0.01–5%), a nonrenewable resource vital for semiconductors and magnetic resonance imaging technologies, yet conventional extraction methods falter at low-concentrations (<0.1%) due to thermodynamic inefficiencies.[6–9]

Current separation technologies face sustainability trade-offs. Solvent absorption, though effective for bulk CO_2 and H_2S removal, consumes 30–40% of processing energy for solvent regeneration and generates corrosive waste.[10] Cryogenic distillation, while achieving high helium purity (99.999%), incurs prohibitive costs for lean reserves (<0.1% He) due to energy-intensive liquefaction.[11] These limitations underscore the urgency for energy-efficient alternatives. Membrane-based separation has gained traction as a low-carbon solution, offering continuous operation without chemical additives and modular scalability suited to decentralized gas fields.[12,13] Among membrane configurations, hollow fiber modules dominate industrial adoption due to their intrinsic self-supporting architecture, unmatched packing densities (up to 10^4 m^2 m^{-3}), ease of scale-up, and superior mechanical resilience compared to spiral-wound and plate-and-frame modules.[14]

Suojiang Zhang

Suojiang Zhang is a member of the Chinese Academy of Sciences (CAS) and president of Henan University. His research interests focus on green chemical engineering, new energy, and materials. He has already broken through the common scientific challenges in the basic theory and engineering scaling up of ionic liquids, developed several original technologies for green energy and low-carbon processes, and successfully achieved industrialization. His achievements in green process engineering are recognized through awards, including the Second-Class Prize of the State Natural Science Award, the Second-Class Prize of the State Technological Innovation Award, and the TWAS Award in Chemistry.

The evolution of polymeric hollow fiber membranes (HFMs) for natural gas treatment traces back to the 1970s with asymmetric cellulose acetate HFMs, achieving a CO_2/CH_4 selectivity of 12–15 but succumbing to plasticization at CO_2 partial pressures >5 bar (Fig. 1).[10,15,16] A paradigm shift occurred in 1994 when polyimide-based HFMs (Medal, Air Liquide) doubled CO_2/CH_4 selectivity to 20–25 while resisting hydrocarbon-induced plasticization.[16] By 2020, HFM systems accounted for 18% of global natural gas processing capacity, with over 500 installations treating >200 billion m^3 annually. These industrial deployments now demonstrate high-efficiency decarbonization, resource valorization, and extreme-condition resilience. For instance, ADNOC's Habshan facility achieves 99% CO_2 removal from 10 MMSCFD streams with <2% CH_4 loss, Evonik's helium-selective HFMs (He/CH_4 selectivity >150) enable economic extraction from sources containing <2% He, Air Products' methane recovery modules, and UBE's H_2S-tolerant polyimide HFMs handle >30 000 ppm H_2S streams without performance decay. These field-proven capabilities establish HFMs as essential components for achieving net-zero emissions targets, specifically in carbon capture applications and helium recovery from unconventional resources. However, persistent challenges associated with plasticization and physical aging phenomena necessitate fundamental innovations in advanced membrane materials.

Despite these advances, existing reviews inadequately address the material–process–performance interplay specific to natural gas treatment scenarios. Prior studies predominantly focused on generic fabrication techniques or broad gas separation applications.[17–23] For instance, Chung *et al.* (2012) detailed phase-inversion principles for HFM formation, with applications spanning CO_2 capture, H_2 production, and desalination,[24] while Othman *et al.* (2018) pioneered the analysis of dual-layer HFMs, emphasizing coextrusion fabrication and comparative advantages over single-layer designs.[25] Kujawski *et al.* (2020) systematically categorized asymmetric, thin-film composites and mixed-matrix HFMs, correlating transport mechanisms with performance,[17] and Yong *et al.* (2021) advanced theoretical frameworks linking spinning parameters to membrane morphology and gas separation efficiency in applications like air separation and propylene/propane splitting.[26] Recent studies, such as Imtiaz *et al.* (2022) on braid-reinforced HFMs and Lau *et al.* (2024) on surface modification techniques, further expanded the technical repertoire.[15,27] However, these studies lack dedicated focus on natural gas treatment, particularly in addressing two critical challenges: (1) the intrinsic relationship between the hierarchical structure of HFMs and their gas separation performance remains unclear, particularly regarding natural gas sweetening under complex gas source conditions and helium extraction from low-concentration sources, and (2) the microscopic mechanisms of aging in polymeric HFMs, along with their plasticization behaviors and anti-plasticization strategies under high CO_2 and light/heavy hydrocarbon exposure, require further elucidation.

This review bridges these gaps by providing a comprehensive analysis of HFMs tailored for natural gas treatment. We begin by elucidating the configuration of asymmetric HFMs and the

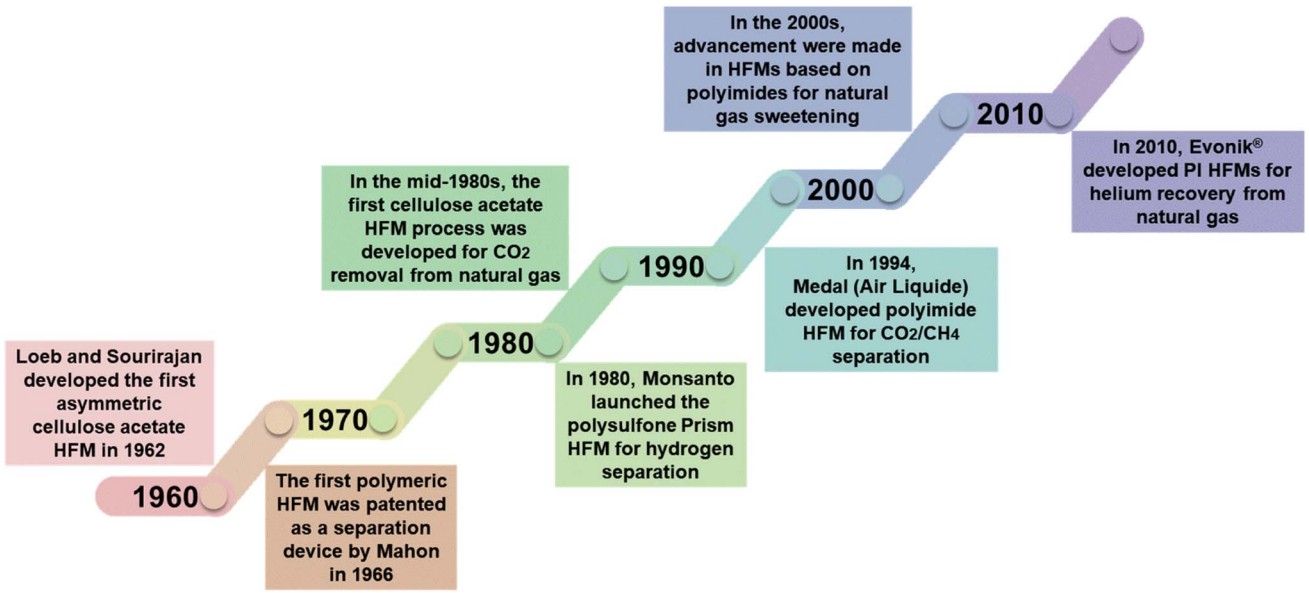

Fig. 1 Milestones in commercial HFM development for natural gas treatment.

fundamental mechanism governing gas transport, followed by a critical evaluation of fabrication methods (*e.g.*, co-extrusion, dip-coating, and interfacial polymerization) and post-modification strategies. Subsequently, we critically analyze advanced polymer materials, including cellulose acetate, polysulfone, polyimides, thermally rearranged polymers, and carbon molecular sieves, specifically engineered for acid gas removal and helium recovery. Challenges such as nanoporous transition layer collapse, physical aging, and plasticization are examined alongside emerging solutions like crosslinking and hybrid matrix designs. Finally, we propose a sustainability-driven roadmap for future research, emphasizing scalability, lifecycle assessment, and alignment with decarbonization goals (Fig. 2). By integrating material innovation with industrial practicality, this work advances HFM technology toward sustainable natural gas valorization.

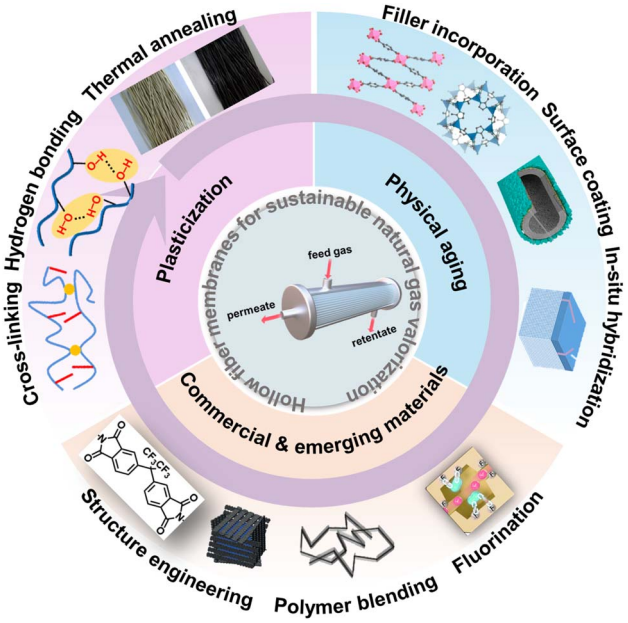

Fig. 2 Schematic diagram of emerging innovations in polymeric hollow fiber membranes for sustainable natural gas valorization.

2 Fundamentals of gas permeation in hollow fiber membranes

Gas transport mechanisms in membranes critically depend on membrane microporosity and gas–material interactions.[28] The solution-diffusion mechanism prevails in polymeric membranes, where separation arises from differential dissolution and diffusion through transient free-volume elements (Fig. 3a). By contrast, pore-mediated mechanisms govern gas transport in porous membrane architectures (Fig. 3b), including molecular sieving *via* steric exclusion in micropores, surface diffusion driven by adsorbed-phase transport, and limited-selectivity flows such as Knudsen or Poiseuille diffusion.[29] Crucially, polymeric HFMs primarily exploit solution diffusion within their dense selective layers, while pore-based mechanisms dominate in nanostructured materials like polymer-derived carbon molecular sieves (CMSs) or nanocomposites incorporating engineered nanoporous fillers.

An integrally asymmetric HFM achieves optimal separation performance through a carefully designed multilayer structure, as shown in Fig. 4a. The membrane consists of three fundamental layers: (1) a macroporous support layer (100–300 μm thick, 60–80% porosity) that provides mechanical stability while contributing less than 5% of total transport resistance; (2) a mesoporous transition layer (1–10 μm thick, 1–50 nm pore size) that serves two critical functions which gradually bridges the large pores of the support with the dense selective layer to prevent delamination and regulates solvent exchange kinetics

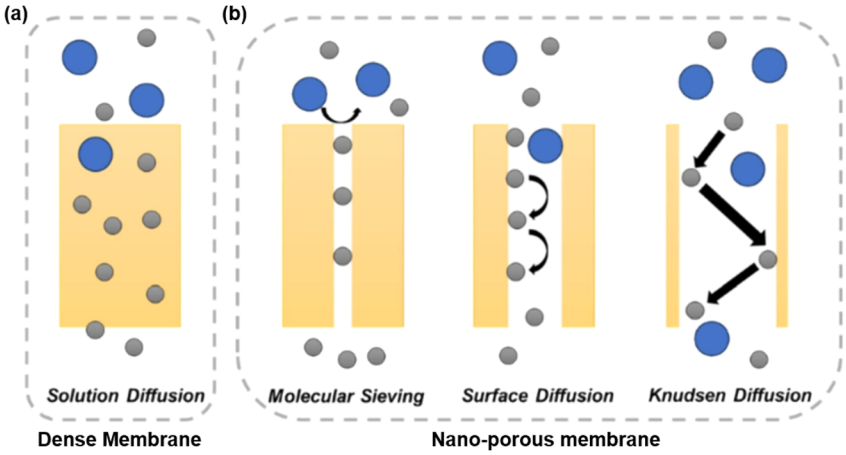

Fig. 3 Schematic for gas transport mechanisms of (a) solution diffusion and (b) molecular sieving, surface diffusion, and Knudsen diffusion. Reproduced with permission from ref. 28 and Copyright 2024, Elsevier.

during phase inversion for facilitating formation of defect-free selective layers; (3) an ultrathin dense selective skin layer (10–1000 nm thick) where molecular sieving primarily occurs. Some advanced configurations may include additional protective coatings (*e.g.*, 10–1000 nm silicone rubber) to heal surface defects, particularly for membranes operating under harsh conditions.[13] This hierarchical architecture enables more than 95% of the separation to occur at the selective layer while maintaining excellent mechanical properties.[30]

Gas permeation through the dense selective layer of polymeric HFMs normally follows the solution-diffusion mechanism. In this process, gas molecules first adsorb onto the membrane high-pressure upstream surface, then diffuse through the polymer matrix *via* thermally activated jumps between transient free-volume elements driven by a concentration gradient and finally desorb into the low-pressure downstream side as permeate. The steady-state gas flux (Q_i) for component i is expressed as:[31]

$$Q_i = \frac{P_i A \Delta P}{L} = \frac{\Delta P}{\left(\frac{L}{P_i A}\right)}$$

where P_i is permeability (Barrer, 1 Barrer $= 10^{-10}$ cm^3 (STP) cm cm^{-2} s^{-1} cmHg^{-1}), A is effective membrane area (cm^2), L is the membrane skin layer thickness (cm), and ΔP is the trans-membrane pressure difference (cmHg).

Permeability (P) is the product of the solubility coefficient (S, cm^3 (STP) cmHg^{-1}) and diffusivity coefficient (D, cm^2 s^{-1}):

$$P = S \times D$$

For HFMs with ultrathin skin layers ($L < 1$ μm), permeance (P/L) is preferred and expressed in gas permeation units (GPU, 1 GPU $= 1 \times 10^{-6}$ cm^3 (STP) cm^{-2} s^{-1} cmHg^{-1}).[32,33] Solubility favors gases with high condensability and strong polymer–penetrant interactions (*e.g.*, quadrupole interactions in polar

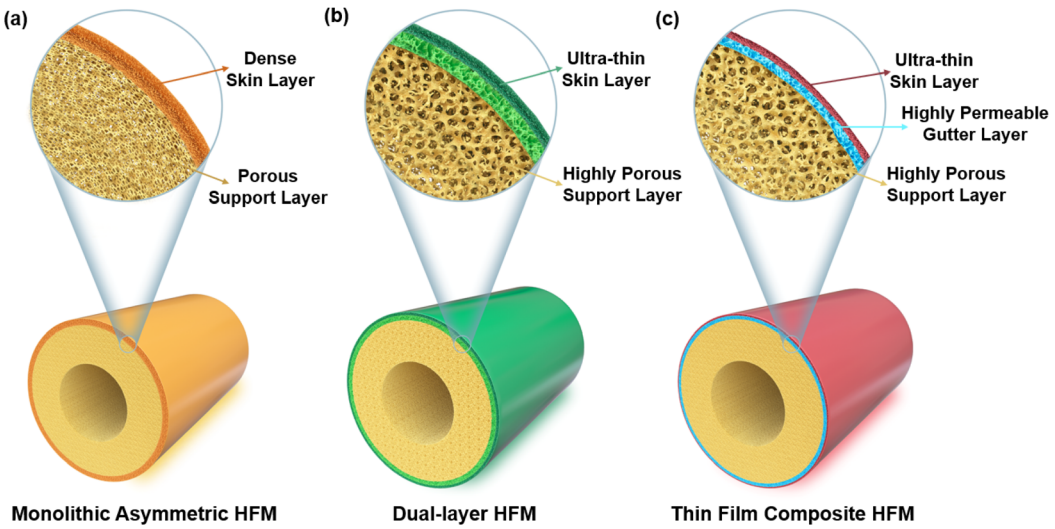

Fig. 4 Schematic of (a) monolithic asymmetric, (b) dual-layer, and (c) thin film composite HFMs.

polymers).[34] Diffusivity dominates in glassy polymers, where rigid chains create narrow free-volume distributions, preferentially passing smaller molecules.[35] Enhancing diffusivity requires smaller penetrant size, larger/more frequent free-volume elements, and increased polymer chain mobility.[34] The ideal selectivity of two gases is defined as follows:[36]

$$\alpha_{A/B} = \frac{(P/L)_A}{(P/L)_B} = \left(\frac{S_A}{S_B}\right) \times \left(\frac{D_A}{D_B}\right)$$

where $(P/L)_A$ and $(P/L)_B$ denote the gas permeance of gases A and B, respectively, and S_A/S_B and D_A/D_B represent the solubility and diffusivity selectivity, respectively.

Polymeric HFMs exhibit an intrinsic permeability–selectivity trade-off.[37] Modifying polymers to enlarge free-volume elements often disproportionately benefits larger molecules (*e.g.*, CH_4 over CO_2), decreasing selectivity.[38] This limitation arises from the inability to simultaneously increase free-volume size and narrow size distribution.[35] The empirical upper-bound relationship quantifies this trade-off:[35]

$$P_i = k\alpha_{ij}{}^n$$

where P_i is permeability of the faster gas (Barrer), α is selectivity (P_i/P_j), and n is the slope dependent on gas-pair molecular diameters (d_i and d_j):[39]

$$\frac{-1}{n} = \left(\frac{d_j}{d_i}\right)^2 - 1 = \left[\frac{d_j + d_i}{d_i{}^2}\right](d_j - d_i)$$

The coefficient k incorporates solubility and polymer free-volume distribution:[40]

$$k^{-1/n} = \frac{S_i}{S_j} S_i{}^{-1/n} \exp\left\{\frac{1}{n}\left[b - f\left(\frac{1-a}{RT}\right)\right]\right\}$$

where S_i and S_j are the solubility coefficients for gases i and j, $a = 0.64$ (universal constant), $b = 11.5$ (glassy polymers), and f is the polymer specific constant (52.633 kJ mol^{-1} for the 1991 upper bound and 59.234 kJ mol^{-1} for the 2008 upper bound).[31]

Molecular sieving in membrane-based gas separation operates through a well-defined activated diffusion mechanism that integrates two synergistic governing principles.[41] First, steric exclusion effects arise from the precise size matching between gas molecules and membrane pore apertures, creating molecular-level filtration. Second, adsorption potential develops through specific interactions between gas molecules and pore walls, including van der Waals forces, electrostatic interactions, and surface chemistry effects.[41] This dual-control mechanism establishes a distinct size-dependent transport behavior with three characteristic regimes. In the preferential transport regime, where gas molecules possess kinetic diameters substantially smaller than the pore dimensions, van der Waals interactions dominate, leading to enhanced surface adsorption and subsequent surface diffusion.[42] The transition regime occurs when molecular dimensions approach the pore size, where steric repulsion creates substantial energy barriers that must be overcome by thermal activation.[42] Finally, the exclusion regime emerges when molecular sizes exceed pore dimensions, resulting in near-complete rejection with selectivity factors exceeding 10^3.[41] These fundamental transport principles remain universally applicable across molecular sieve materials, with particular relevance to polymer-derived CMS hollow fiber membranes. Through pyrolysis at controlled temperatures, these membranes develop precisely tuned ultramicroporous networks that exhibit exceptional molecular discrimination. The pyrolysis process carefully balances carbonization and activation to optimize pore size distribution while maintaining structural integrity, enabling targeted separation of gas pairs such as CO_2/CH_4 and He/CH_4 with industrial-scale efficiency.

Surface diffusion achieves gas separation through two coupled processes: selective adsorption of components with higher affinity onto pore surfaces and surface migration *via* hopping between adsorption sites.[43] This mechanism dominates CO_2 separation in microporous membranes under low-temperature/high-pressure conditions, where enhanced adsorption selectivity drives performance.[43] Membranes leveraging surface diffusion contain slightly larger micropores than molecular sieves. The surface diffusion coefficient (D_s) follows Gilliland's model:[44]

$$D_s = D_0 e^{-\frac{E_a}{RT}}$$

$$E_a = a \times q$$

where D_0 is the pre-exponential factor, governed by adsorbed molecule vibration frequency and adsorption site spacing. E_a reflects the activation energy required for adsorbed molecules to jump between adjacent sites. a is a dimensionless scaling factor ($0 < a < 1$), relating to surface energy heterogeneity. q is the isosteric heat of adsorption representing adsorption strength. This formula reveals a critical trade-off: stronger adsorption (higher q) enhances selectivity but reduces mobility by increasing E_a, necessitating balanced q values in CO_2 separation membranes to avoid kinetic trapping.

The governing flow regime in porous membranes is determined by the Knudsen number ($Kn = \lambda/r$), where λ is the mean free path and r is the pore radius. Poiseuille flow dominates when $Kn \ll 1$ ($r > 10\lambda$), described by:[45]

$$G = \frac{r^2}{8\mu} \frac{(p_f - p_p)}{L} \frac{p_{avg}}{RT}$$

$$p_{avg} = (p_f + p_p)/2$$

where p_f and p_p are the feed and permeate pressures, respectively, L is pore length, μ is gas viscosity, and G is the viscous flow. Knudsen flow prevails when $Kn \ll 1$ ($r < 10\lambda$), where gas molecules collide primarily with pore walls rather than other molecules. Collisions scattered in random directions and the separation factors for gas molecules are inversely proportional to the square root of molecular weight.[46] Both transport mechanisms provide inherently low selectivity due to insufficient molecular discrimination.[45] Consequently, membranes

operating predominantly in Knudsen or Poiseuille regimes are technologically unsuitable for high-performance gas separation application.

The solution-diffusion mechanism governs gas transport in dense polymeric layers, providing high selectivity while being fundamentally constrained by the permeability–selectivity trade-off. Molecular sieving (*e.g.*, in carbon molecular sieves) enables precise size discrimination, although it requires sub-nanometer pore-size control (<0.7 nm) and exhibits vulnerability to aging-induced structural degradation. Surface diffusion enhances selectivity for condensable species (*e.g.*, CO_2), but experiences diffusivity–selectivity compromises due to strong sorption hysteresis. Knudsen and Poiseuille flows yield separation factors below 5 ($\alpha < 5$), rendering them inadequate for molecular-level separation. Consequently, advanced membrane architectures integrate complementary mechanisms: ultrathin solution-diffusion skins enabling high-flux permeation, combined with molecular-sieving domains or surface-functionalized nanopores to achieve selectivity enhancement under aggressive industrial feed gas.

3 Configuration and fabrication of hollow fiber membranes

Building upon the gas transport fundamentals established in Section 2, where solution-diffusion selectivity and interconnected free-volume elements govern molecular separation, the architectural design of industrial hollow fiber membranes strategically translates these principles into three performance-optimized configurations. Asymmetric HFMs leverage ultrathin selective skins to maximize permeance while minimizing resistance from the graded porous substructure (Fig. 4a). Dual-layer HFMs intrinsically decouple structural functions: cost-effective supports ensure mechanical robustness while high-performance selective layers determine separation efficiency, with interfacial engineering providing synergistic integration to prevent delamination (Fig. 4b).[47] TFC HFMs exploit nanoscale selective layers (<500 nm) deposited on optimized supports, enabling independent tuning of transport and mechanical properties (Fig. 4c).[48] Collectively, these configurations demonstrate how hierarchical structure–property relationships translate fundamental transport theory into industrial performance.

3.1 Asymmetric outer selective layer HFMs

The dry-jet/wet-quench spinning process remains the cornerstone for fabricating asymmetric outer selective layer HFMs, offering unparalleled control over membrane morphology and separation performance.[49] This process typically involves sequential steps: (1) formulating polymer dope and bore fluids, (2) co-extrusion through a spinneret, (3) controlled phase separation in the air gap and coagulation bath, and (4) post-spinning treatment.[50] Critical performance determinants include dope formulation, processing parameters (*e.g.*, air gap length and take-up speed), and post-treatment protocols, which collectively dictate the selective layer thickness, substructure

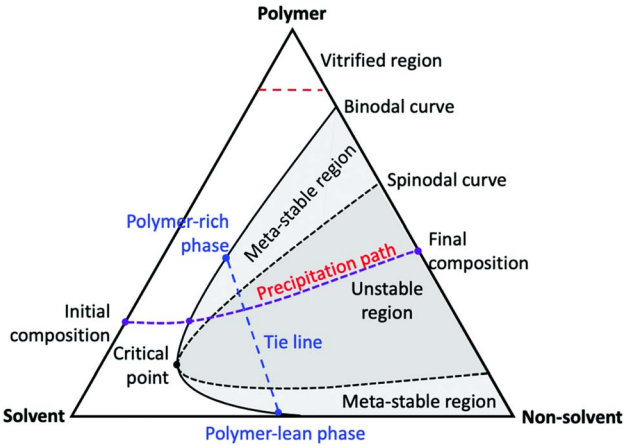

Fig. 5 Schematic ternary phase diagram of polymer–solvent–non-solvent systems. Reprinted with permission from ref. 23, Copyright 2022, the Royal Society of Chemistry.

porosity, and mechanical strength.[51–54] Dope optimization is guided by ternary phase diagrams (Fig. 5), where spinnable compositions lie near the binodal line in the one-phase region.[55] For instance, solutions with balanced polymer concentrations (18–27%) and viscosity enable sufficient chain entanglement for fiber integrity while maintaining spinnability.[56] The solvent volatility ratio, controlled by blending low-volatility (*e.g.*, *N*-methyl-2-pyrrolidone) and high-volatility solvents (*e.g.*, tetrahydrofuran), precisely regulates solvent evaporation kinetics and phase inversion dynamics.[53,54] Increasing air gap length accelerates solvent evaporation, leading to the formation of denser and thicker skin layer.[54] Conversely, elevated coagulation bath temperatures accelerate solvent/non-solvent exchange rates, favoring porous substructures with lower mass transfer resistance.[49]

Li *et al.*[57] developed defect-free 6FDA-*m*$PDA_{0.9}$-$TFMB_{0.1}$ copolyimide HFMs for He enrichment by optimizing polymer concentration and phase separation kinetics. At <25 wt% polymer concentrations, porous substructures achieved a He permeance of 72.1 GPU, while >30 wt% concentrations produced slightly thick skin layers (200–300 nm), reducing permeance by 35%. By tuning air gap height (5 cm) and coagulation bath composition (water/ethanol = 70 : 30), the resultant HFMs exhibited a burst pressure of 10.5 MPa and He/CH_4 selectivity of 178. Remarkably, these membranes retained structural integrity under extreme conditions (750 PSIA mixed-gas feeds, −40 °C), showing a He permeance of 46 GPU and He/CH_4 selectivity of 429.[58] Similarly, Kosuri *et al.*[59] engineered a Torlon® HFM for high-pressure CO_2 separation by suppressing macrovoids through an increased polymer concentration (28 wt%) and elevated dope temperatures (60 °C). The optimized membranes achieved a CO_2/CH_4 selectivity of 39.6 under 1100 PSIA feed pressure at 35 °C, demonstrating suitability for industrial high-pressure natural gas upgrading.

Polymer blending offers a cost-efficient approach to enhance hollow fiber membrane (HFM) performance by combining complementary properties of base polymers and additives. Yong *et al.*[60] demonstrated this strategy by incorporating 5–15

wt% PIM-1 into Matrimid® dopes, achieving ultrathin selective layers (30–70 nm) (Fig. 6a). The blend HFMs exhibited CO_2 permeance increases of 78% (153.4 GPU) and 146% (212.4 GPU) at 5 wt% and 10 wt% PIM-1 loadings, respectively, while maintaining CO_2/CH_4 selectivity >26. Further optimization with 15 wt% PIM-1, 95 : 5 NMP : H_2O bore fluid, and silicone rubber coating improved CO_2 permeance to 243.2 GPU and CO_2/CH_4 selectivity to 34 by sealing surface defects (Fig. 6b and c). However, PIM-1's limited solubility constrained the blending ratio. To address this critical limitation, Jue *et al.*[61] developed a triple-orifice spinneret for coextruding the PIM-1 dope with a protective sheath layer of 1-butanol/THF (Fig. 6d). This approach reduced volatile solvent THF evaporation relative to the polymer dope directly exposed to air, yielding defect-free asymmetric HFMs with a 3–6 μm skin layer. These HFMs initially achieved a CO_2 permeance of 540 GPU and selectivity of 25, stabilizing at 360 GPU, and CO_2/CH_4 selectivity of 23 after two-month aging. In a complementary additive approach, Hu *et al.*[62] incorporated 0–12 wt% polyethylene glycol (PEG) as a CO_2-philic additive into dope solution for Matrimid® 5218 HF spinning. Increasing the PEG concentration accelerated phase separation during membrane formation, producing hollow fibers with higher porosity and thinner selective skins and

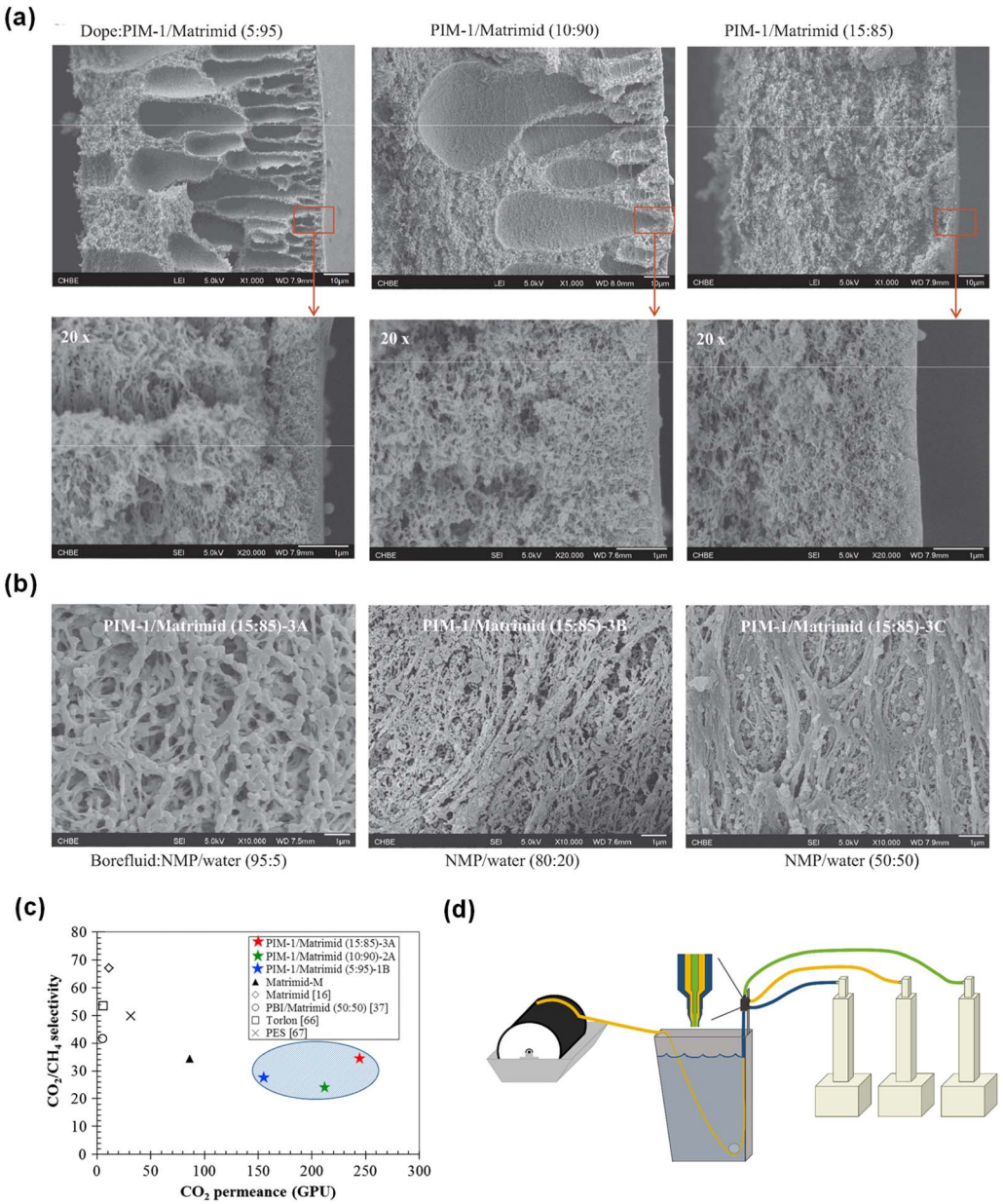

Fig. 6 (a) Selective layer thickness *versus* PIM-1 content in PIM-1/Matrimid® blend HFMs. (b) Inner surface morphology of PIM-1/Matrimid® (15 : 85 ratio) fibers fabricated with different bore fluids. (c) CO_2/CH_4 separation performance of PIM-1/Matrimid blends HFMs. Reprinted with permission from ref. 59, Copyright 2013, Elsevier. (d) Spinning apparatus employing a triple-orifice spinneret for simultaneous coextrusion of sheath fluid (blue), polymer dope (yellow), and bore fluid (green). Reprinted with permission from ref. 60, Copyright 2017, Elsevier.

elevating CO_2 permeance from 21 GPU (neat Matrimid®) to 37 GPU (12 wt% PEG).

3.2 Dual-layer hollow fiber membranes

Dual-layer hollow fiber membranes (DLHFMs), integrating a high-performance, expensive, thin selective outer layer and a cheap, porous support layer, have emerged as a cost-effective strategy for gas separation by minimizing the use of high-performance polymers.[63] Fabrication of DLHFMs, primarily *via* co-extrusion spinning, requires precise control over dope rheology of the two distinct polymer solutions, air gap distance, and coagulation bath composition to ensure interfacial adhesion and structural integrity.[64] Key challenges include delamination from mismatched shrinkage rates and defective interfaces caused by shear stress variations during co-extrusion.[65] Jiang *et al.*[66] demonstrated that increasing the inner dope polymer concentration (polysulfone: 25% to 30%) reduced shrinkage during phase inversion, enabling robust adhesion of the outer Matrimid® layer. Optimized conditions yielded DLHFMs with a CO_2 permeance of 11 GPU and CO_2/CH_4 selectivity of 40. Raza *et al.*[67] further revealed a V-shaped CO_2 permeance-air gap relationship (minimum at 5 cm) and Λ-shape CO_2/CH_4 selectivity profile (peak at 5 cm) for cellulose triacetate (CTA)–cellulose diacetate (CDA)/CTA dual-layer HFMs, achieving 45 GPU CO_2 permeance and 30.3 CO_2/CH_4 selectivity at a 1 mL min^{-1} outer dope flow rate with a take-up speed of 15 m min^{-1}, double the permeance without sacrificing selectivity compared to single-layer counterparts.

Surface modification and crosslinking strategies significantly enhance separation performance of DLHFMs. Li *et al.*[68] fabricated DLHFMs using coextrusion technology where both inner and outer layers consisted of polyethersulfone (PES) with different polymer concentrations of 23 wt% and 35 wt%, respectively. These HFMs subsequently underwent surface modification through a three-step chemical treatment: chloromethylation, sulfonation, and silver ion exchange. The

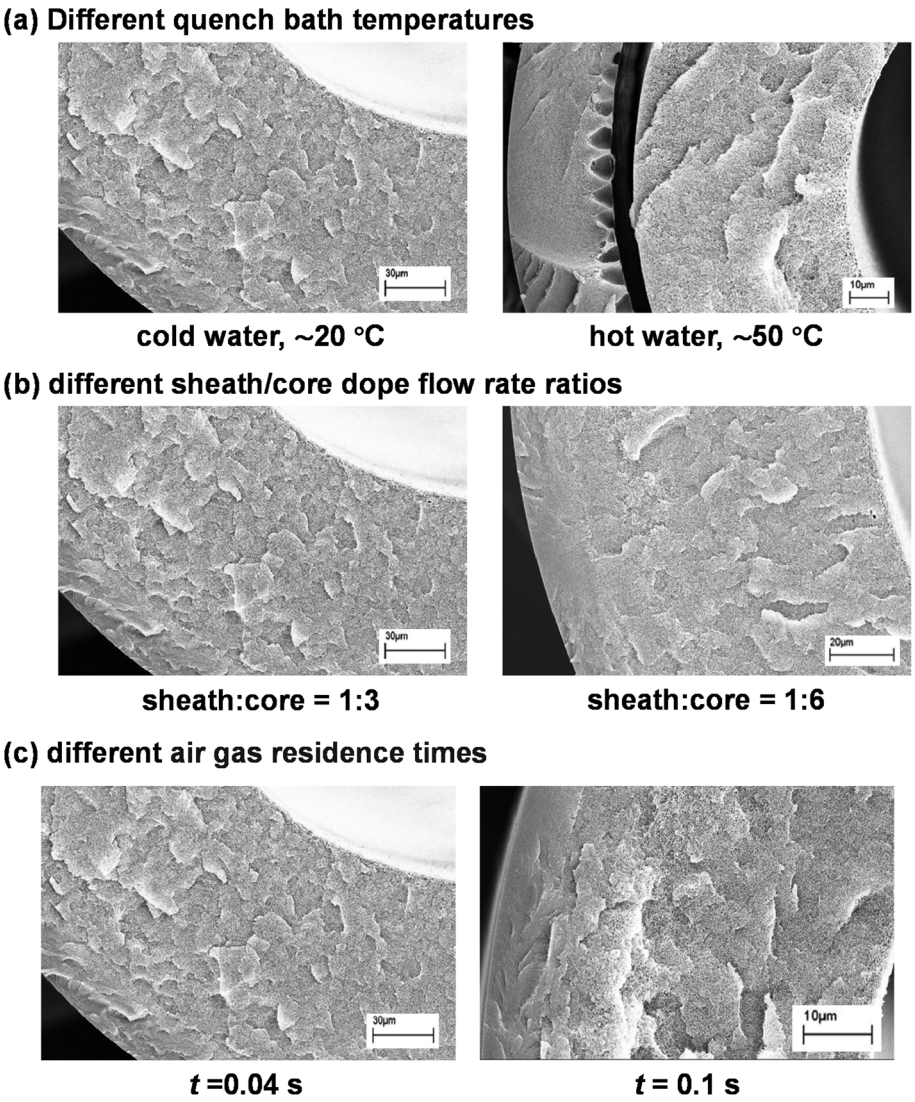

Fig. 7 SEM images of PDMC/Torlon® composite hollow fibers under varied processing conditions: (a) quench bath temperature, (b) sheath/core flow ratio, and (c) air gap residence time. Reprinted with permission from ref. 69, Copyright 2013, American Chemical Society.

incorporated silver ions selectively enhanced CO_2 transport *via* quadrupole interactions, achieving an exceptional CO_2/CH_4 selectivity of 118 with a CO_2 permeance of 25.1 GPU. Liu *et al.*[69] chemically crosslinked the outer 6FDA-durene-*m*PDA layer of 6FDA-durene-*m*PDA/PES DLHFMs with *p*-xylylenediamine, forming rigid networks that boosted CO_2/CH_4 selectivity to 101 despite reduced CO_2 permeance (28.3 GPU). Ma *et al.*[70] engineered ester-cross-linkable Torlon®/6FDA-DAM : DABA (3 : 2) DLHFMs, where optimized quench bath temperature (50 °C), sheath/core flow ratios (1 : 3), and an air gap residence time of 0.04 s yielded defect-free fibers (Fig. 7a–c). Crosslinked hollow fibers demonstrated stable CO_2 permeance (40 GPU) and CO_2/CH_4 selectivity (39) under 100 PSIA feeds (CO_2/CH_4, 50/50 v/v) containing 1000 ppm toluene, highlighting industrial viability.

Filler incorporation into DLHFMs enhances performance through complementary mechanisms: molecular sieving *via* filler nanopores improved gas affinity through functional groups (*e.g.*, amine–CO_2 interactions) and tuned polymer chain packing that suppresses non-selective pathways. However, filler loading exceeding 5 wt% can create interfacial defects, necessitating surface modifications for uniform dispersion.[71] For instance, Khan *et al.*[72] incorporated polyethyleneimine (PEI)-functionalized bimetallic MOF (PEI@HKUST-1(Cu, Mg)) exclusively into the outer layer dope with polysulfone (PSf) utilized as a polymer in both inner and outer dopes for DLHFM spinning. The amine groups from PEI-MOFs enhanced CO_2 affinity while open metal sites combined with high porosity provided additional CO_2 binding sites and transport channels. The synergistic design promoted rapid CO_2 permeation, yielding 75% higher CO_2 permeance (28 GPU) and 85% improved CO_2/CH_4 selectivity (51) compared to unmodified PSf HFMs.

3.3 Thin film composite HFMs

Thin-film composite (TFC) HFMs overcome limitations of monolithic designs through a decoupled fabrication strategy. First, a porous polymeric support (*e.g.*, polysulfone and polyimide) is formed *via* phase inversion. Subsequently, an ultra-thin selective layer (at 1 μm thickness) is deposited *via* dip coating or interfacial polymerization.[73–76] This sequential approach enables independent optimization of support morphology (pore size, porosity, and surface chemistry) and selective layer properties (thickness, crosslink density, and functionality), achieving unprecedented permeance-selectivity combinations.[77,78] Dip coating-recognized as the most industrially viable technique-involves immersing HFM substrates into coating solutions. Final membrane performance critically depends on substrate properties, pre-wetting protocols and process parameters including solution concentration, withdrawal speed, and curing conditions.[79–81] Qin *et al.*[82] fabricated polysulfone (PSf)/poly (4-vinylpyridine) (4-PVP)/silicon rubber (SR) multilayer composite membranes *via* dip-coating. They controlled PSf substrate's pore size by adjusting diethylene glycol (DEG) content (nonsolvent additive) during phase inversion. Pre-wetting proved essential for preventing coating penetration into large-pore substrates. Using optimized DEG content with 5 wt% and pre-wetting, they achieved a CO_2 permeance of 92 GPU and CO_2/CH_4 selectivity of 29 at 25 °C and 200 psi. Li *et al.*[83] optimized polyvinylamine/polyvinyl alcohol (PVAm/PVA) coatings on PSf HFMs using orthogonal experimental design. Key parameters include a 20 wt% PSf concentration and PEG-400 additive. The resulting composite HFMs with a selective layer thickness of 160 nm delivered a CO_2 permeance of 52 GPU with a CO_2/CH_4 selectivity of 24 under mixed-gas conditions (CO_2/CH_4, 40/60, v/v), outperforming conventional cellulose acetate HFMs.

Material innovations in TFC HFMs now strategically address two critical industry barriers: reducing the environmental footprint of membrane manufacturing and overcoming permeance-selectivity trade-offs. Theodorakopoulos *et al.*[84] demonstrated these by engineering P84 co-polyimide/Pebax-1657 composite HFMs. They replaced toxic *N*-methyl-2-pyrrolidone (NMP) with greener γ-butyrolactone (GBL) in support HF fabrication, reducing solvent toxicity while maintaining spinnability. Simultaneously, graphene nanoplatelets (GNPs) incorporated into both support and selective layers enhanced separation performance. The resulting (G_{Green}/Pebax + GNPs)/P84 composite HFMs achieved a CO_2/CH_4 selectivity of 82 and He/N_2 selectivity of 20, with CO_2 and He permeances of 3GPU and 2.7GPU respectively under binary gas testing (1.3 bar, 25 °C). Complementing solvent and nanofiller innovations, novel polymer architecture could also enhance TFC HFM separation performance. Gutiérrez-Hernández *et al.*[85] coated PIM-1 with 11% side-chain substitution as a selective layer on PP-HF impregnated PDMS. The B-PIM-1/PDMS/PP HFMs achieved a CO_2 permeance of 650 GPU and CO_2/CH_4 selectivity of 14.

Interfacial polymerization (IP) enables ultra-thin (<500 nm), chemically tailored selective layers through controlled monomer diffusion.[59,86] Jo *et al.*[87] polymerized trimesoyl chloride (TMC) and 1,3-cyclohexanebis-methylamine (CHMA) on PSf HFMs, where the CHMA concentration governed crosslinking density. At 1.0% CHMA/0.5% TMC, the membrane achieved a CO_2 permeance of 25 GPU and CO_2/CH_4 selectivity of 28. Choi *et al.*[88] fabricated a He-selective membrane *via* *m*-phenylenediamine (*m*-PDA)/TMC IP on PAN supports, followed by PTMSP gutter layer deposition. The resultant membrane exhibited a He permeance of 46.2 GPU and He/CH_4 selectivity of 11.9. Future directions integrate machine learning (ML) to optimize curing kinetics and monomer ratios. Neural networks trained on experimental datasets could predict optimal dip-coating parameters for target selectivity.[89,90] ML models can bridge molecular design with process engineering, accelerating the development of TFC HFMs for extreme industrial conditions (*e.g.*, high-pressure natural gas feeds).

3.4 Complementary strategies and synergistic innovations

Asymmetric, dual-layer, and thin-film composite hollow fiber membranes play complementary roles in natural gas valorization through distinct economic and operational advantages. Dual-layer configurations strategically combine high-performance selective polymers such as 6FDA polyimides with economical supports like polysulfone, reducing material costs

by 40–60% while preserving over 90% separation efficiency. This design excels in cost-sensitive applications including marginal natural gas fields. Asymmetric membranes deliver superior stability under aggressive conditions, where cross-linked variants withstand CO_2 partial pressures exceeding 500 PSIA, making them indispensable for bulk acid gas removal. Thin-film composites enable module-level retrofitting, where advanced coatings (*e.g.*, PIM-1 derivatives) achieve permeance enhancement without infrastructure modification, enabling economical helium recovery from sub-0.3% sources.

Emerging synergies bridge different membrane architectural paradigms through cross-technology integration. Electrospinning also offers significant potential for fabricating HFMs with tunable nanofibrous architectures and enhanced surface functionalities, enabling novel transport pathways for gas separation. Recent advances in coaxial spinning techniques demonstrate promising routes toward scalable hollow fiber production, complementing conventional fabrication methods.[91] Hybrid fabrication enables co-extruded dual-layer supports to host ultrathin selective skins *via* interfacial polymerization, eliminating delamination while enhancing molecular sieving. Concurrently, machine learning-guided architecture selection dynamically matches membrane types to feed conditions: thin-film composite HFMs for CO_2-dominant streams and asymmetric HFMs for helium enrichment scenarios. These fabrication innovations directly enable the advanced polymers discussed in Section 4, where hierarchical structures (*e.g.*, DLHFMs) maximize the performance of emerging materials like TR polymers and CMSs. Collectively, these pathways advance hollow fiber membranes toward adaptive, economically viable gas separation systems that maintain industrial robustness while addressing evolving sustainability imperatives.

4 Select relevant polymers for HFMs

Polymeric materials underlie the vast majority of hollow fiber membrane configurations, with fabrication processes requiring balanced solution processability, mechanical robustness, and gas separation performance. Key commercially established

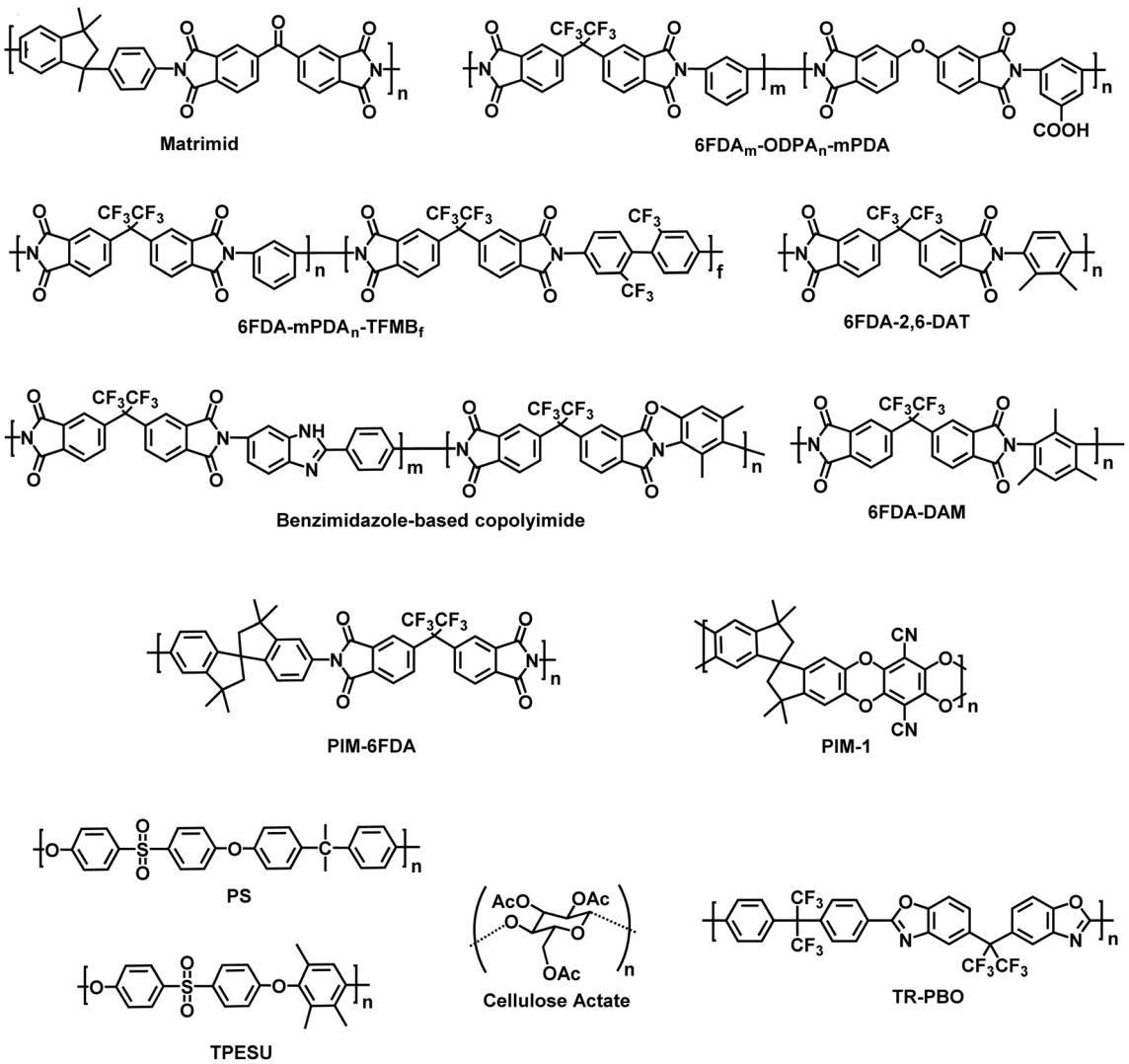

Fig. 8 Representative chemical structures of HFM polymers.

materials include cellulose acetate (CA), polysulfone (PS), and polyimide (PI), alongside emerging candidates like thermally rearranged (TR) polymers and carbon molecular sieves (CMSs) (Fig. 8). These polymers exhibit critical structural attributes: (1) chain rigidity (*e.g.*, aromatic rings in PI and fused bicyclic units in PIMs) that enhances size-sieving selectivity *via* restricting polymer chain mobility; (2) asymmetric/contorted backbones (*e.g.*, spirobisindane in PIM-1) that create interconnected free-volume elements for fast gas transport; (3) functional groups (*e.g.*, sulfone groups in PS and imide rings in PI) that confer chemical stability under harsh conditions; and (4) solvent compatibility, enabling dissolution and phase inversion in defect-free hollow fibers.[92–94] This section systematically evaluates relevant HFM materials by elucidating their intrinsic transport properties, analyzing advanced modification strategies, and identifying key challenges for sustainable manufacturing.

4.1 Cellulose acetate (CA)

Cellulose acetate (CA), derived from renewable cellulose *via* acetylation, has been a cornerstone material for gas separation membranes since the 1980s due to its low cost, tunable hydrophilicity, and inherent CO_2 affinity.[95–97] The degree of substitution (DS = 2.4–2.8) critically governs membrane performance: cellulose triacetate (CTA) exhibits higher free volume compared to partially acetylated CA, enhancing CO_2 permeance to 10–15 GPU but increasing susceptibility to CO_2-induced plasticization.[98,99] Bulky acetyl groups disrupt cellulose's crystalline structure, creating amorphous regions that facilitate gas diffusion while maintaining mechanical stability.[100] Recent advances focus on optimizing spinning parameters and post-treatments to enhance the gas separation performance of CA-based HFMs.[101,102] Pak *et al.*[103] demonstrated that reducing the tetrahydrofuran/ethanol (THF/EtOH) ratio in spin dopes from 3 : 1 to 1 : 1 slowed the precipitation rate, forming denser skin layers with 30% fewer defects. Coupled with a 15 cm air gap for enhancing molecular orientation, PDMS-coated CA HFMs achieved a CO_2 permeance of 12.9 GPU and CO_2/CH_4 selectivity of 43.8 at 3 bar, surpassing unmodified membranes by 70% in selectivity. Mubashir *et al.*[104] revealed a V-shaped permeance-air gap relationship and Λ-shaped selectivity profile for CA HFMs, with optimized take-up speeds yielding a CO_2/CH_4 selectivity of 7.9. PDMS coating outperformed thermal annealing (120 °C) by sealing macrovoids, improving CO_2/CH_4 selectivity by 70.9%.

Incorporating nanoparticles into cellulose acetate matrices produces mixed matrix hollow fiber membranes (MMHFMs) with enhanced CO_2/CH_4 separation performance. Strategic manipulation of spinning parameters minimizes interfacial voids in these MMHFMs, further improving their gas separation efficiency. For instance, Mubashir *et al.*[105] fabricated NH_2-MIL-53(Al)/CA MMHFMs containing 15 wt% MOF by optimizing take-up speed and air-gap distance. They observed that increasing take-up speed improved ideal selectivity by 40% due to shear-induced molecular alignment, while air-gap variations produced distinct "*V*" and "Λ" patterns. Under optimal conditions (12.2 m min^{-1} take-up speed, 5.0 cm air gap), the membrane achieved a CO_2/CH_4 ideal selectivity of 16.0 with a CO_2 permeance of 6.7 GPU at 25 °C and 3 bar feed pressure. In a follow-up study using design of experiments, they demonstrate that increasing permeance testing temperature from 30 °C to 50 °C reduced the CO_2/CH_4 separation factor of MMHFMs due to accelerated polymer chain relaxation, whereas elevating feed pressure from 3 to 15 bar and CO_2 feed composition from 15 to 42.5 vol% enhanced separation performance. Feed pressure emerged as the dominant factor, reducing CH_4 permeance by 32% while marginally lowering CO_2 permeance, yielding a maximum CO_2/CH_4 separation factor of 14.4 at 15 bar, 30 °C, and 15 vol% CO_2.[106] Similarly, Sunder *et al.*[102] fabricated NH_2-MIL-125(Ti)/CTA MMHFMs *via* a 1 cm air-gap process, where dual PDMS coating reduced surface defects but introduced permeance loss (35%) due to thicker coating. The modified membranes exhibited a CO_2/CH_4 ideal selectivity of 6.87 and CO_2 permeance of 26.46 GPU.

4.2 Polysulfone (PS)

Polysulfone (PS), with its alternating sulfone ($-SO_2^-$) and biphenyl groups, serves as an industry-standard polymer for gas separation membranes due to exceptional thermal stability, chemical resistance, and mechanical robustness under high-pressure conditions.[107] The electron-withdrawing sulfone groups promote dense chain packing, resulting in a low fractional free volume of approximately 5%. Consequently, while CO_2 permeance remains at 20–30 GPU, size-sieving selectivity for small molecules is enhanced.[108–110] Commercial PS variants, synthesized *via* nucleophilic substitution between 4,4′-dichlorodiphenylsulfone (DCDPS) and bisphenols, achieve tunable properties through backbone modifications.[111] For instance, Yong *et al.*[112] synthesized poly(trimethyl phenylene ether sulfone) (PESU) by replacing one diphenyl sulfone unit with a bulky and rigid 1,2,4-trimethylbenzene moiety, which introduced additional free volume and suppressed chain relaxation. The resultant HFMs exhibited a CO_2 permeance of 85.1 GPU and CO_2/CH_4 selectivity of 35.5 at 3.5 bar, with aging rates reduced by 60% compared to conventional PS.

The gas separation performance of PS HFMs is highly sensitive to spinning parameters and post-treatment conditions. Lower dope solution temperatures (T_d) and coagulation bath temperatures (T_c) slow solvent-non-solvent exchange rates, promoting denser skin layers with reduced macrovoid formation.[66] Liu *et al.*[113] demonstrated that reducing T_d from 35 °C to 3 °C and T_c from 25 °C to 7 °C minimized finger-like macrovoids, yielding membranes with a CO_2 permeance of 53.5 GPU. However, unmodified PS HFMs exhibit low selectivity ($CO_2/CH_4 \approx 1.24$), necessitating post-coating treatments. Silicone rubber (PDMS) coating (3 wt%) on optimized PS HFMs enhanced selectivity to 39.4 while maintaining CO_2 permeance at 31.9 GPU. Roslan *et al.*[114] further showed that increasing the polysulfone polymer concentration (from 15 to 35 wt%) in spin dopes reduced gas permeance by 45% but improved CO_2/CH_4 selectivity by 150% due to denser membrane structures. Multilayer coating (3 wt% PDMS + 3 wt% Pebax® 1657) on PS

HFMs achieved optimal performance (CO_2 permeance of 21.12 GPU and a CO_2/CH_4 selectivity of 34.28), outperforming single-layer PDMS by 87% in permeance.

PS serves as an ideal matrix for mixed-matrix and thin-film composite HFMs. Khan *et al.*[115] incorporated 0.5 wt% ZIF-8 into PSf HFMs, leveraging molecular sieving and CO_2-philic open metal sites to achieve a CO_2 permeance of 47.75 GPU and CO_2/CH_4 selectivity of 25.7. Sasikumar *et al.*[116] engineered amine-modified SiO_2 and ZIF-8 MM-HFMs with Pebax®-1657 coating, where amine groups enhanced CO_2 affinity, yielding a CO_2 permeance of 41.15 GPU and CO_2/CH_4 selectivity of 22.25. Sharif *et al.*[117] developed PES-based nanocomposite HFMs with PVP/PDMS/SiO_2 skin layers, achieving a CO_2/CH_4 selectivity of 45, CO_2 permeance of 102 GPU, and tensile strength of 58 MPa, a 40% improvement over pristine PS.

4.3 Polyimide (PI)

Aromatic polyimides (PIs), synthesized *via* polycondensation of aromatic dianhydrides and diamines, are distinguished by their highly tunable gas separation properties and exceptional thermal/mechanical stability, positioning them as premier materials for natural gas purification.[118,119] Successful fabrication of polyimide HFMs critically hinges on precise control over polymer architecture, molecular weight distribution, and purity during dope preparation, in which only small variations in the polymer structure can significantly impact the ability to form a workable dope.[55] Random copolymers with minimal block/branch structures prevent localized aggregation and maintain homogeneous solution rheology for stable fiber spinning. Conversely, block or branched architectures promote gelation due to enhanced intermolecular associations and topological entanglements in solution, driven by microphase separation tendencies of chemically distinct segments. Optimal molecular weight balances chain entanglement for fiber integrity against excessive viscosity, while residual monomers and cyclic oligomers must be eliminated to avoid phase separation during spinning. These material parameters collectively govern solvent–polyimide interactions.

Soluble homopolyimides, such as 6FDA/DAM and Matrimid®, are commonly used due to their ability to form workable dopes.[55] The rigid backbone architecture, characterized by kinked structures (*e.g.*, the phenylindane moiety in Matrimid®) and bulky substituents (*e.g.*, hexafluoroisopropylidene groups in 6FDA), generates a tunable free-volume fraction (15–25%) that directly governs gas transport.[92,120,121] For instance, Matrimid® 5218 (BTDA-DAPI) achieves a CO_2 permeance of 17.7 GPU and CO_2/CH_4 selectivity of 24.3 at 2 bar, surpassing polyethersulfone HFMs by 50% in CO_2/CH_4 selectivity under comparable conditions.[121,122] Cao *et al.*[123] developed 6FDA-2,6-DAT HFMs *via* NMP-based spinning, showing an initial CO_2 permeance of 300 GPU. Physical aging reduced permeance to 76 GPU over 185 days due to free-volume collapse, but mixed-gas tests ($CO_2/CH_4 = 50/50$) showed stabilized permeance at 59 GPU with a CO_2/CH_4 selectivity of 40, highlighting industrial viability. Gutiérrez-Hernández *et al.*[124] fabricated 6FDA-TMPD TFC HFMs using polypropylene hollow fibers as porous supports and highly permeable PDMS as a blocking layer to mitigate the intrusion of 6FDA-TMPD. The membrane achieved a CO_2 permeance of 54.5 GPU and CO_2/CH_4 selectivity of 13.9 in CO_2/CH_4 (50 : 50 vol%) gas mixtures, demonstrating stable performance up to 30 bar.

Spinning parameter optimization (*e.g.*, dope solvent selection and polyimide concentration) critically impacts the polyimide HFM microstructure and gas separation performance. Hachisuka *et al.*[125] demonstrated that diethylene glycol dimethyl ether (DGDE) as the good solvent produces defect-free 6FDA-BAAF HFMs with ultrathin selective layer, achieving a CO_2 permeance of 550 GPU and CO_2/CH_4 selectivity of 27. In contrast, NMP generates finger-like macrovoids due to rapid phase separation, reducing selectivity by 35%. Qin *et al.*[126] optimized shear rates during 6FDA-durene/*m*PDA fiber spinning, yielding defect-free structures with a CO_2 permeance of 53.3 GPU and CO_2/CH_4 selectivity of 42.9 after post-PDMS coating, outperforming dense films by 29% in selectivity. Besides, lower molecular weight PIs require adjusting dope formations to maintain spinnability. Xu *et al.*[127] increased the polymer concentration and reduced ethanol/$LiNO_3$ additives to suppress phase separation, achieving defect-free HFMs with a CO_2/CH_4 selectivity of 22.7 (29% higher than dense films). This highlights the inverse relationship between molecular weight and required polymer concentration for optimal fiber formation.

4.4 Thermally rearranged polymers

Thermally rearranged (TR) polymers are typically derived from *ortho*-functionalized polyimide precursors (*e.g.*, hydroxyl-containing polyimides) *via* controlled pyrolysis (400–450 °C),[128,129] forming rigid heterocyclic structures (*e.g.*, polybenzoxazoles, PBO) with ultra-high fractional free volume.[130,131] Their bimodal pore architecture combines ultramicropores (<7 Å) for precise molecular sieving with interconnected micropores (>10 Å) for rapid gas transport, positioning them ideally for CO_2/CH_4 separation.[132] However, substructure collapse during pyrolysis thickens selective layers and reduces permeance by up to 40% *versus* precursors.[133] Recent advances mitigate this through precursor engineering and crosslinking strategies.

Kim *et al.*[134] minimized substructure collapse by first conducting thermal imidization at 300 °C on hydroxyl poly(amic acid) precursors, stabilizing the fiber morphology, before thermal rearrangement at 450 °C for 60 min. The resulting TR-PBO HFMs achieved a CO_2 permeance of 1938 GPU and CO_2/CH_4 selectivity of 14 with a 2 μm selective layer, retaining 60% higher permeance than conventional TR-HFMs. To enhance selectivity while preserving permeance, Fan *et al.*[135] designed phenolphthalein-modified 6FDA-DAP : DAM (1 : 2) precursors. Sub-T_g crosslinking (*via* lactone ring opening) locked the polymer network, preventing pore coalescence during pyrolysis. Subsequent thermal rearrangement at 400 °C generated slit-like ultramicropores, yielding a CO_2 permeance of 436.22 GPU and CO_2/CH_4 selectivity of 30.63, a 120% selectivity jump over non-crosslinked TR analogs without permeance sacrifice. These collective advances demonstrate that TR polymer performance hinges critically on preserving pore architecture integrity during

rearrangement, a challenge now addressable *via* molecular-scale precursor control.

4.5 Carbon molecular sieves

Carbon molecular sieve (CMS) HFMs achieve exceptional gas separation performance through their hierarchical pore architecture, where micropores (7–20 Å) facilitate rapid transport while ultramicropores (<7 Å) function as molecular sieves.[136,137] Pore structure modulation strategies include precursor design, pyrolysis condition optimization, and post-synthesis modifications.[138–141] Vu *et al.*[142] demonstrated that vacuum pyrolysis of 6FDA/BPDA-DAM at 550 °C yielded CMS membranes with a CO_2 permeance of 25–30 GPU and CO_2/CH_4 selectivity of 73–85, outperforming Matrimid®-derived CMSs with a CO_2 permeance of 11–13 GPU and CO_2/CH_4 selectivity of 69–83. Precise pyrolysis temperature control adjusts ultramicroporous gateways for target molecules. Zhang *et al.*[143] demonstrated that pyrolysis >875 °C refines ultramicropores to 4.0–4.5 Å (Fig. 9a and b), creating "selective adsorption sites" within a less selective carbon matrix. The carbon/carbon mixed-matrix (CCMM) membranes pyrolyzed at 900 °C demonstrated unprecedented separation performance, achieving a CO_2/CH_4 selectivity of 3650 and He/CH_4 selectivity of 16 700. This exceptional performance results from the synergistic combination of size exclusion and adsorption affinity, which surpasses the diffusion-limited selectivity of traditional CMS materials. Structural characterization by WAXRD and Raman spectroscopy (Fig. 9c and d) confirms that the CMS samples consist of highly disordered amorphous domains.

Precursor-derived chemistry and post-synthesis functionalization fine-tune microporosity and gas separation performance of HFMs. Kamath *et al.*[144] retained 18.5% fluorine ($-CF_3$ groups) in 6FDA-DETDA : DABE CMS HFMs *via* a two-stage pyrolysis protocol: crosslinking at 370 °C followed by carbonization at 500 °C under argon, which expanded free volume while narrowing pore size distribution. The resultant membranes exhibited a CO_2 permeance of 552 ± 28 GPU, with a CO_2/CH_4 selectivity of 37.0 ± 4. Wu *et al.*[145] fluorinated partially carbonized $6FDA_{0.9}$-$ODPA_{0.1}$-*m*PDA HFMs, polarizing the pore wall through C–F bonds. This strengthened H_2 interaction and reduced effective pore size,

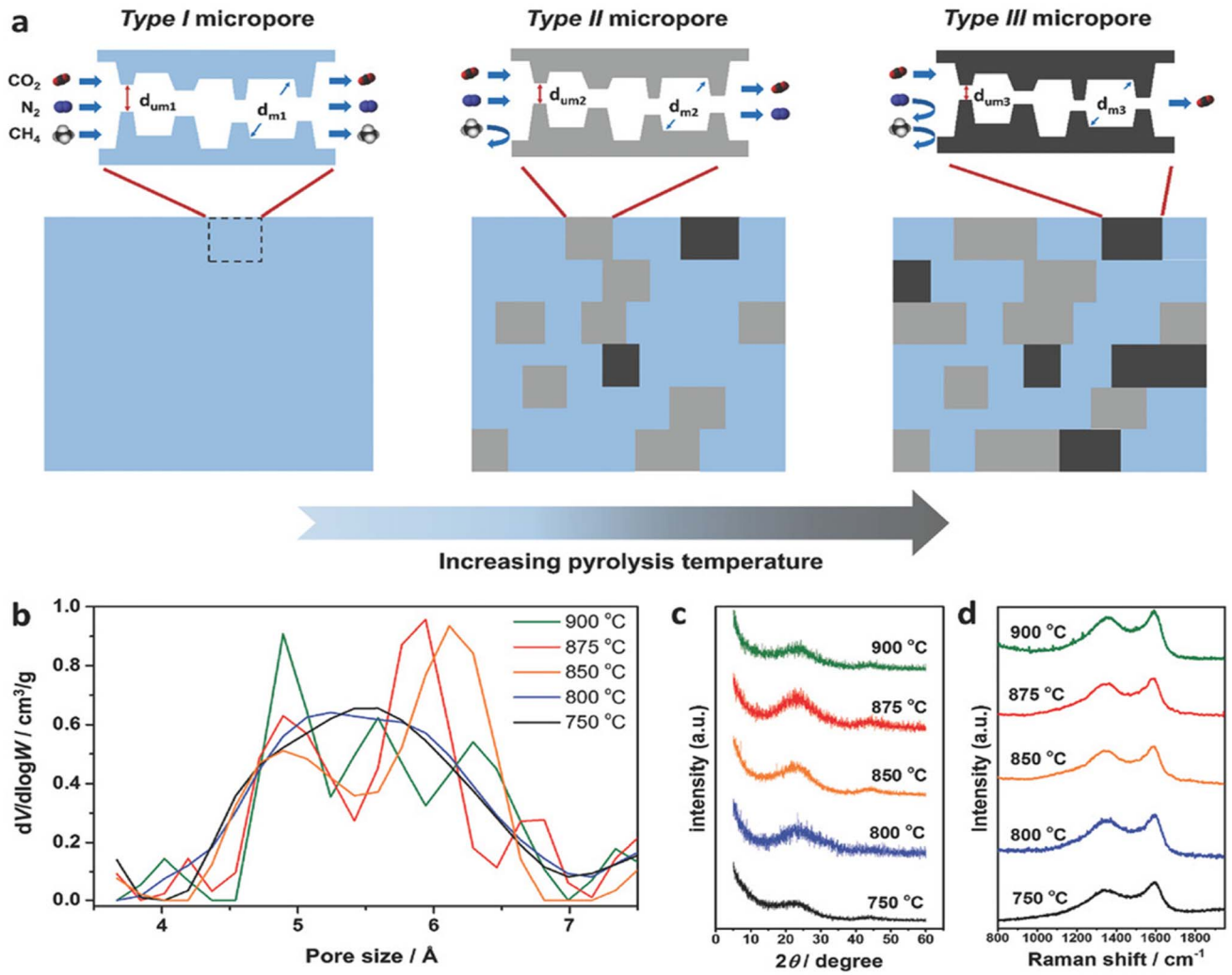

Fig. 9 (a) Structural evolution of carbon/carbon mixed-matrix membranes with pyrolysis temperature (750–900 °C). (b) Pore-size distribution, (c) WAXRD, and (d) Raman spectra of CCMS membranes. Reprinted with permission from ref. 141, Copyright 2017, John Wiley and Sons.

boosting He/H_2 selectivity from 3.1 to 9.7, while maintaining He permeance >100 GPU ($\alpha(He/CH_4) = 2193$).

CMS membranes demonstrate unparalleled robustness under extreme conditions. Zhang *et al.*[146] reported 6FDA/BPDA (1 : 1)-DAM CMS HFMs maintaining CO_2/CH_4 selectivity ~60 under supercritical natural gas feeds (1800 PSIA, 50% CO_2, and 500 ppm C_7 hydrocarbons) across 200 h and −50 to 100 °C thermal cycles. Lei *et al.*[147] developed cellulose-derived CMS HFMs *via* ionic liquid spinning, where the precursor dried at 140 °C reduced average pore size from 6 to 4.9 Å. Despite a 22% decrease in CO_2 diffusivity, the narrowed pores amplified size exclusion, achieving a CO_2/CH_4 ideal selectivity of 917 (2 bar) and mixed-gas separation factor of 131 (50 bar, 60 °C).

Composite CMS membranes represent the future of membrane technology by enabling tunable separation properties and substantial cost reductions. By integrating economically engineered supports (*e.g.*, P84) with high-performance polymers, precursor hollow fibers with dense skin layers achieve a 25-fold material cost reduction compared to monolithic or ceramic supports. Cao *et al.*[148] demonstrated this through multi-layer asymmetric CMS HFMs fabricated by coating P84 supports with 6FDA : BPDA-DAM polyimide followed by controlled pyrolysis. Optimizing the polymer solution concentration, coating humidity, and pyrolysis temperature yielded CMS-675 membranes with a CO_2/CH_4 selectivity of 58.8 and CO_2 permeance of 310 GPU under CO_2/CH_4 (50 : 50) mixed-gas feed at 35 °C. Building on this, Cao *et al.*[149] developed co-extruded composite CMS membranes using 6FDA-DAM (sheath) and Matrimid® (core), eliminating post-carbonization defect repairs. Pyrolyzed at 675 °C, these membranes achieved an enhanced CO_2/CH_4 selectivity of 64.3 and CO_2 permeance of 232 GPU, outperforming their single-layer counterparts by 11% in selectivity while maintaining industrial-grade permeance.

4.6 Materials development and transformative pathways

The century-spanning development of hollow fiber membrane materials reflects the balance between permselectivity thresholds, long-term stability, and sustainable manufacturability (Fig. 10 and Tables S1–S3). Cellulose acetate established the paradigm of bio-sourced membranes yet remains fundamentally constrained by plasticization vulnerabilities; polysulfone delivers exceptional mechanical resilience while undergoing progressive aging-induced performance decay; aromatic polyimides achieve high-precision selectivity through engineered free-volume control, though their intricate synthesis hinders circular economy integration; while thermally rearranged polymers and carbon molecular sieves transcend Robeson upper bounds *via* tailored ultramicroporosity, their energy-intensive activation processes contradict decarbonization imperatives.

These inherent limitations now drive three transformative innovations: computational materials design integrating multiscale modeling approaches to optimize the permselectivity–stability–manufacturability trade-offs; bio-hybrid systems integrating enzymatic recycling pathways for closed-loop polymer recovery; and stimuli-responsive membranes featuring dynamically tunable free-volume architectures. This convergence positions next-generation HFMs as adaptive platforms for precision gas separation, where programmable molecular architectures enable autonomous optimization of gas transport across fluctuating natural gas compositions.

5 HFM performance evaluation

Hollow fiber membranes suffer from three major performance deteriorations: plasticization by penetrant-induced chain mobilization that swells free volume and reduces selectivity; physical aging from gradual free-volume contraction that decreases permeance; and transition-layer collapse originating from capillary forces during phase inversion or pyrolysis stress during carbonization. This section elucidates the underlying mechanisms of these phenomena, links them to performance decline, and analyzes stabilization strategies.

5.1 Plasticization

Plasticization in polymeric HFMs refers to the performance degradation caused by highly soluble components (*e.g.*, CO_2

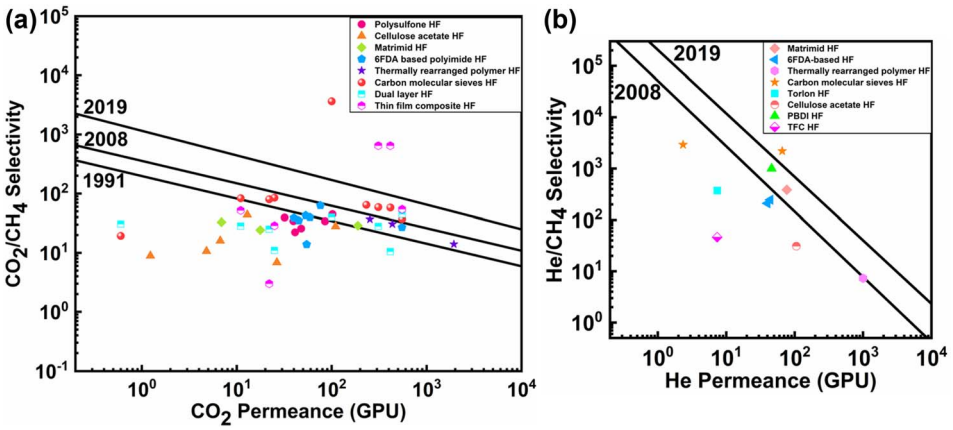

Fig. 10 Gas permeance-selectivity upper bound plots for (a) CO_2/CH_4 and (b) He/CH_4 separation. All evaluated materials assume fabrication with 1 μm thick selective layers. Benchmark data incorporate state-of-the-art polymeric HFMs, with comprehensive comparisons in Tables S1–S3.

and hydrocarbons) under high-pressure or high-concentration feed streams.[150,151] These penetrants act as molecular lubricants, swelling the polymer matrix by increasing inter-chain spacing and segmental mobility, thereby enhancing gas diffusivity while compromising size-sieving selectivity (Fig. 11).[38,152,153] This phenomenon is particularly prevalent in natural gas processing, where CO_2 partial pressures exceeding 100 PSIA induce membrane swelling, leading to diminished gas recovery rates and operational reliability.[154–156] Glassy polymers such as 6FDA-based polyimides exhibit dual selectivity mechanisms (diffusivity and solubility-driven), making them promising for CO_2/CH_4 separation.[157] However, their strong CO_2 affinity renders them susceptible to plasticization under mixed-gas conditions, where competitive sorption effects exacerbate performance decline.[158–160] Commercial materials like cellulose acetate and Matrimid® 5218 also face selectivity loss at elevated CO_2 pressures, restricting their application in high-pressure environments.[161] The reported plasticization pressure hierarchy for common glassy polymers is polysulfone (PSf) > polyethersulfone (PES) > P84 > poly(2,6-dimethyl *p*-phenylene)oxide (PPO) > Matrimid® 5218 (BTDA-DAPI) > cellulose acetate (CA) > cellulose triacetate (CTA).[162] To address this limitation, advanced strategies including cross-linking, post heat-treatment, hydrogen bonding, polymer blending, and using semi-interpenetrating polymer networks have been developed for suppressing plasticization.[158,163–165]

Chemical crosslinking has emerged as a principal strategy for enhancing plasticization resistance (Fig. 14). Five main approaches have been systematically investigated: thermally induced decarboxylation crosslinking, esterification crosslinking, metal ion coordination, amine-mediated nucleophilic crosslinking, and halogen induced radical crosslinking.[166,167] Decarboxylation crosslinking forms stable C–C covalent bonds *via* decarboxylation-induced free radical reactions that restrict polymer chain mobility while maintaining structural integrity under high feed pressures. Li *et al.*[168] demonstrated this using 6FDA-*m*$PDA_{0.65}$-$DABA_{0.3}$-$TFMB_{0.05}$ copolyimide HFMs (Fig. 12a–f). Under ternary $He/CO_2/CH_4$ (0.3/49.5/49.2, v/v/v) feed at 100–600 PSIA, crosslinked HFMs showed minimal permeance variation: He permeance decreased from 13.4 to 9.5 GPU, CH_4 permeance remained stable (0.07–0.08 GPU), and He/CH_4 selectivity declined from 186 to 119. When challenged with hydrocarbon contaminants (propane/heptane), selectivity reductions were limited to 8.7/11.4% at 600 PSIA (Fig. 12g and h), respectively, attributed to the crosslinked polymer structure for preventing polymer chain swelling and alleviating competitive adsorption. Wang *et al.*[169] developed dual thermally crosslinked asymmetric HFMs using 4,4′-diamino-2,2′-biphenyldicarboxylic acid (DCB)-containing copolyimides. The dual crosslinking mechanism combined stable C–C bonds with bulky CF_3 groups from TFMB diamine restricting imide bond rotation, inhibiting transition layer collapse and achieving a skin layer thickness of 1.2 μm. The optimized PI-TFMB-HF@400 membrane demonstrated a He permeance of 25 GPU and He/CH_4 selectivity of 269. Under aggressive ternary feed ($He/CO_2/CH_4$, 0.3/49.7/50, v/v/v), CO_2/CH_4 selectivity decreased by only 24%, while mixed-gas [$He/(CO_2 + CH_4)$] selectivity increased by 80%, showcasing exceptional pressure stability.

Esterification crosslinking creates robust interchain bridges through transesterification, effectively restricting chain mobility and free volume swelling under high pressure conditions. This significantly enhances plasticization resistance while maintaining size-sieving capabilities. Wallace *et al.*[170] engineered ester-crosslinked polyimide (6FDA-DAM : DABA 3 : 2) HFMs, demonstrating that crosslinking temperature more effectively improved plasticization resistance than prolonged treatment duration. The optimized HFMs maintained a stable CO_2/CH_4 selectivity of 28 at 1000 PSIA over 100 hours, with full performance recovery at 200 PSIA, indicating reversible swelling without permanent plasticization. Babu *et al.*[171] extended this

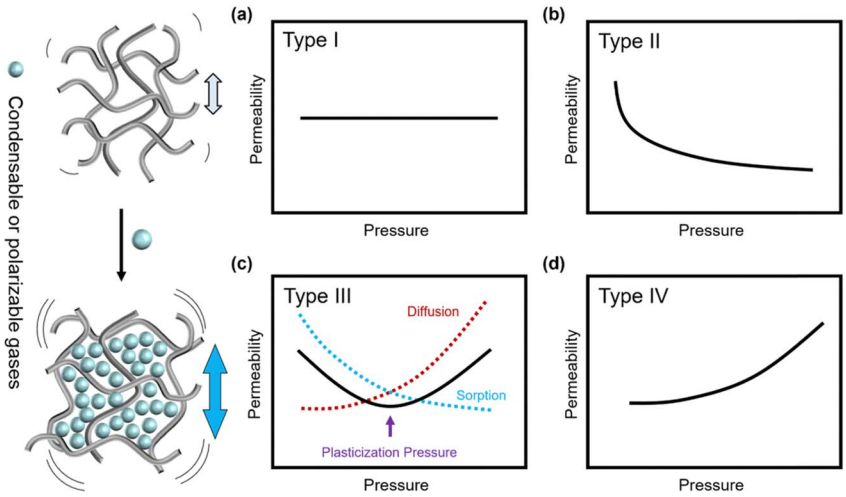

Fig. 11 Schematic illustrating plasticization mechanisms for glassy polymers, demonstrating four different permeability trends based on varying penetrant behaviors. (a) Non-plasticizing with low sorption, (b) non-plasticizing with moderate sorption, (c) highly sorbing, where the plasticization pressure marks the point at which increased diffusion overcomes the reduction in sorption, and (d) highly plasticizing with very high sorption. Reprinted with permission from ref. 154, Copyright 2024, Royal Society of Chemistry.

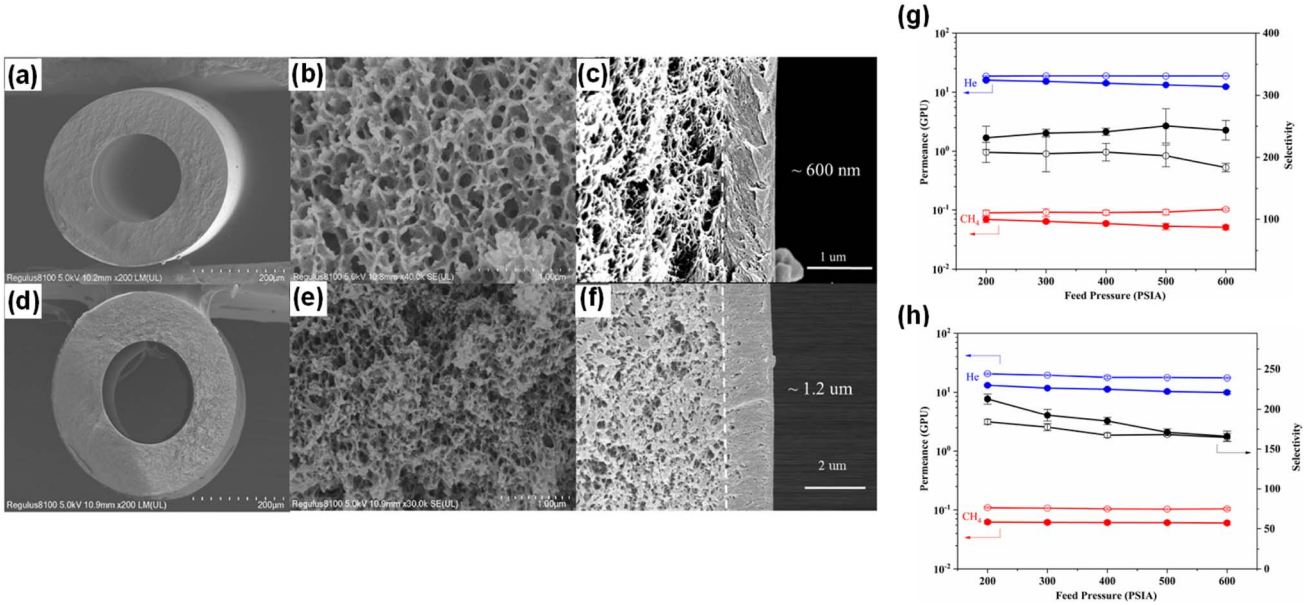

Fig. 12 Structural and performance characterization of crosslinked HFMs. (a–f) SEM images showing preserved substrate porosity and dense skin layer post-crosslinking. Effect of feed pressure on the mixed-gas He and CH_4 permeance and He/CH_4 selectivity of pristine and crosslinked HFMs in ternary (g) He/C_3H_8/CH_4 (0.3/3.0/96.7, v/v/v) and (h) He/*n*-C_7H_{16}/CH_4 (0.3/0.4/99.3, v/v/v). Reprinted with permission from ref. 166, Copyright 2023, Elsevier.

approach to TEGMC (Triethylene Glycol Monoesterified Crosslinkable) HFMs, achieving a H_2S/CH_4 selectivity of 22 under extreme conditions (20% H_2S, 500 PSIA).

To address the risk of transition layer collapse caused by reduced gas permeance in HFMs with ultrathin skin layers, particularly those weakened by thermal crosslinking, Li *et al.*[172] developed polyimide–cerium (PI–Ce) complex HFMs with a 300 nm ultrathin skin layer made from 6FDA-*m*$PDA_{0.65}$-$DABA_{0.3}$-$TFMB_{0.05}$ copolyimide *via* metal ion coordination. This approach enhances plasticization resistance, particularly for helium separation. In a ternary gas mixture (He/CO_2/CH_4, 0.3/49.4/50.3, v/v/v) at 35 °C and feed pressure ranging from 100 to 600 PSIA, the He permeance of the PI–Ce HFM decreased marginally from 29 to 27 GPU, while CH_4 permeance rose slightly from 0.122 to 0.127 GPU. This led to a 10.8% decline in He/CH_4 selectivity (239 to 213) as pressure increased from 100 to 400 PSIA. When heavy hydrocarbons (*n*-C_7H_{16}) were introduced, He permeance dropped by 26.3% (19.8 to 16.5 GPU) and He/CH_4 selectivity decreased by 14.6% (229 to 194) between 100 and 300 PSIA. The robust plasticization resistance of PI–Ce HFMs highlights their potential for helium recovery in harsh natural gas environments. Liu *et al.*[173] incorporated CF_3 groups into polyimide backbones to enhance chain rigidity, producing TFM-PI-CF_3 fibers without skin layer thickening after pyrolysis (200 °C, 2 h; Fig. 13a–f). In contrast, the cross-linked TFM-PI-0 fiber showed a significantly reduced CO_2 permeance of 46 GPU, 2.5 times lower than its pristine non-cross-linked fiber's permeance of ~115 GPU (Fig. 13g), which is consistent with its increased skin thickness (Fig. 13c and d). Under 55 bar feed gas pressure with 50/50 CO_2/CH_4, these CF_3-modified membranes maintained stable CO_2 permeance (~90 GPU) and selectivity (~43). Even when exposed to 250 ppm hydrocarbon contaminants (heptane/toluene), they retained selectivity > 30 at 55 bar, demonstrating exceptional plasticization resistance (Fig. 13h–i).

For amine-mediated nucleophilic crosslinking, amine-rich agents open imide rings *via* carbonyl addition, forming amide linkages. Cao *et al.*[174] demonstrated that immersing 6FDA-2,6-DAT HFMs in *p*-xylenediamine (PXDA)/methanol solution triggers nucleophilic attack on carbonyl groups, generating bis-amide crosslinks. This raised plasticization pressure from 100 PSIA (unmodified and lightly cross-linked) to >200 PSIA, while stabilizing CO_2 permeance at ~20 GPU. Similarly, Ren *et al.*[175] demonstrated that PXDA treatment of 6FDA-ODA/NDA HFMs with immersion times exceeding 1.5 min could achieve plasticization resistance up to 550 PSIA (37.4 atm), as confirmed by FTIR analysis showing conversion of imides to amides. This performance marked a substantial enhancement compared to non-crosslinked membranes that plasticized at 75 PSIA.

Thermal annealing, a cost-effective post-treatment, improves membrane stability by increasing packing density, reducing free volume, and elevating glass transition temperature (T_g).[176,177] Chung *et al.*[178] thermally treated 6FDA-2,6 DAT HFMs at 250 °C for 5 min, minimizing skin layer thickening while suppressing CO_2-induced plasticization. Aged for 60 days, these membranes withstood feed pressures exceeding 500 PSIA, maintaining a stable CO_2 permeance of ~34 GPU. This enhanced stability was attributed to tighter chain packing and a denser skin layer. Dong *et al.*[162] corroborated this by annealing Matrimid® HFMs at 250 °C for 30 min, which retained CO_2 permeance near 20 GPU and a selectivity of ~28 under CO_2/CH_4 (20/80) mixed-gas at 10–35 bar, showing no plasticization.

Hydrogen bonding has emerged as another strategy to restrict chain mobility and counteract plasticization.[71] Kosuri

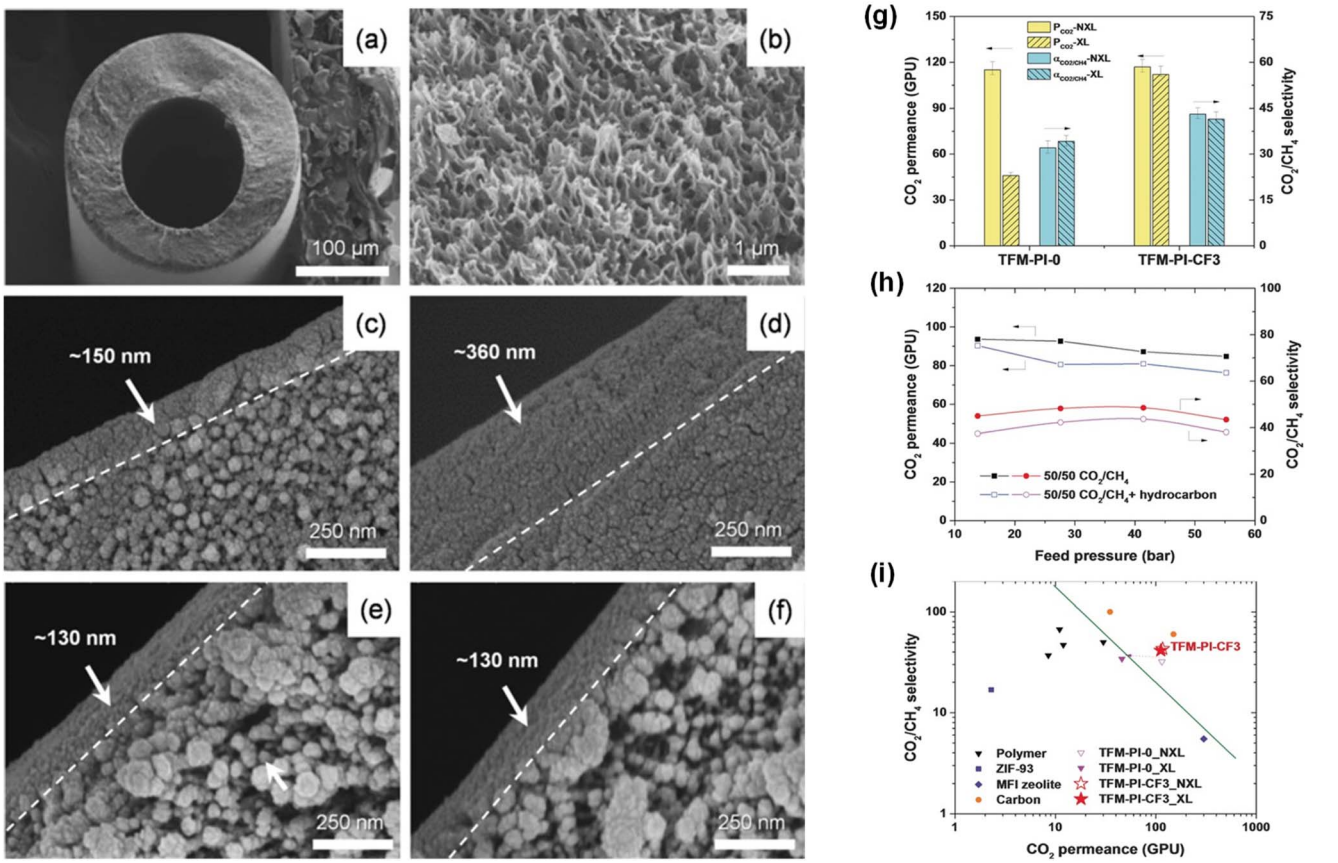

Fig. 13 (a–f) SEM images illustrating CF_3-modified fiber morphology; (g–i) gas separation performance under hydrocarbon-contaminated high-pressure feeds. Reprinted with permission from ref. 171, Copyright 2016, John Wiley and Sons.

et al.[59] fabricated Torlon® HFMs with inter- and intra-chain hydrogen bonds, achieving a CO_2/CH_4 selectivity of 44 (85% of its dense film value of 52). Compared to Ultem® (400 PSIA), Matrimid® (174 PSIA), and 6FDA-DAM : DABA 2 : 1 (PSIA), the Torlon® HFM exhibited superior stability, maintaining constant CO_2 permeance up to 1220 PSIA and a selectivity of 39.6 under supercritical 90% CO_2/10% CH_4 feed. While plasticization typically degrades membrane performance, Liu *et al.*[165] revealed its benefits for CTA HFMs in aggressive natural gas feeds containing H_2S (20 mol%), light hydrocarbons (C_2H_6: 3 mol%; C_3H_8: 3 mol%), and toluene (300 ppm) at 31.3 bar and 35 °C. Plasticization-induced chain mobility elevated CO_2 and H_2S diffusivity (>110 GPU) while maintaining size-sieving selectivity (22–28 over CH_4). This counterintuitive behavior stems from enhanced condensable gas transport through transient free-volume elements without compromising rigid matrix integrity.

5.2 Physical aging

Physical aging describes the gradual structural relaxation of glassy polymers below their glass transition temperature (T_g), where non-equilibrium polymer chains reorganize toward thermodynamic equilibrium.[155,179] This densification process reduces excess free volume, leading to declining gas permeance over time (Fig. 15a).[180] During aging, restricted chain mobility elevates the activation energy for gas diffusion (E_D) and diminishes solubility coefficients due to reduced sorption site availability (Fig. 15b).[181,182] Aging kinetics in HFMs are modulated by thermal history (<1 μm skin layers age faster),[183,184] asymmetric architecture (dense skin/porous support),[185,186] and processing conditions (*e.g.*, quenching rate).[184–187] Strategies to mitigate physical aging in high-free-volume glassy polymers include CO_2 conditioning, nano-filler incorporation (*e.g.*, MOFs, Mxenes, and graphene oxide) and structural reinforcement.[179,188–192]

For instance, Ma *et al.*[193] mitigated physical aging of PDMC hollow fiber membranes through CO_2 conditioning and continuous CO_2/CH_4 feed tests. It was found that periodical 15 PSIG CO_2 conditioning reduced the CO_2 permeance loss of cross-linked HFMs by ~50%, compared to unconditioned ones during a 2300 h aging test. However, the HFM exposed to 200 PSIA 50/50 CO_2/CH_4 continuous feed showed a CO_2 permeance loss of only up to 3%, compared to the 25% loss for samples without continuous mixed gas feed during a 400 h aging test. These results suggest that physical aging may be essentially quenched as long as the membrane remains in contact with a high CO_2 partial pressure feed typical of actual aggressive feeds for which the membrane would be used. Beyond conditioning strategies, nano-fillers mitigate physical aging by restricting polymer chain relaxation through geometric confinement effects. When incorporated into high-free-volume polymers, the porous/lamellar fillers create tortuous diffusion

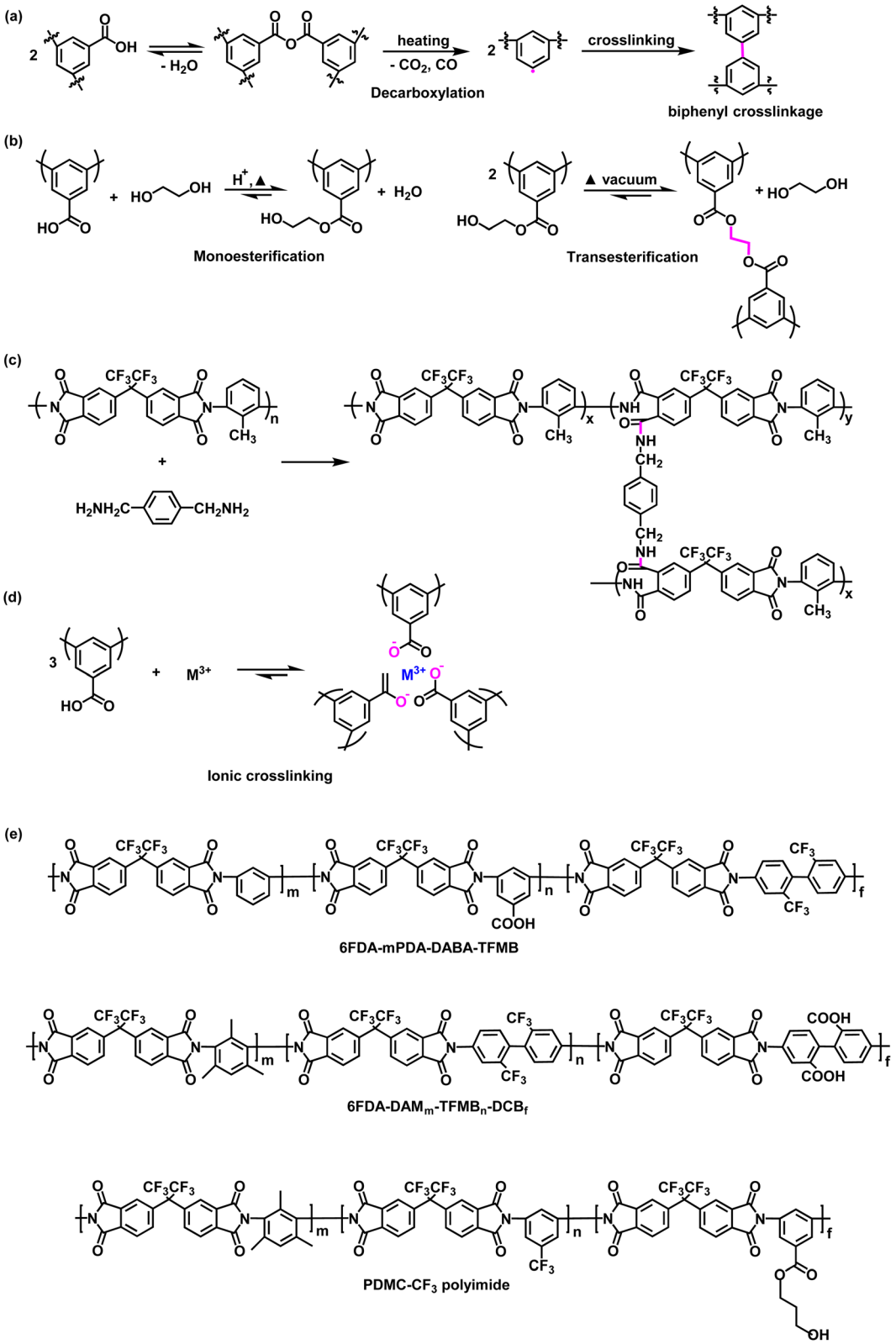

Fig. 14 Summary of strategies for enhancing plasticization resistance in polymer HFMs. Mechanisms include (a) decarboxylation-induced crosslinking, (b) transesterification and ester crosslinking, (c) amine-mediated nucleophilic crosslinking, and (d) ionic crosslinking. (e) Representative chemical structures of the cross-linkable polymers discussed.

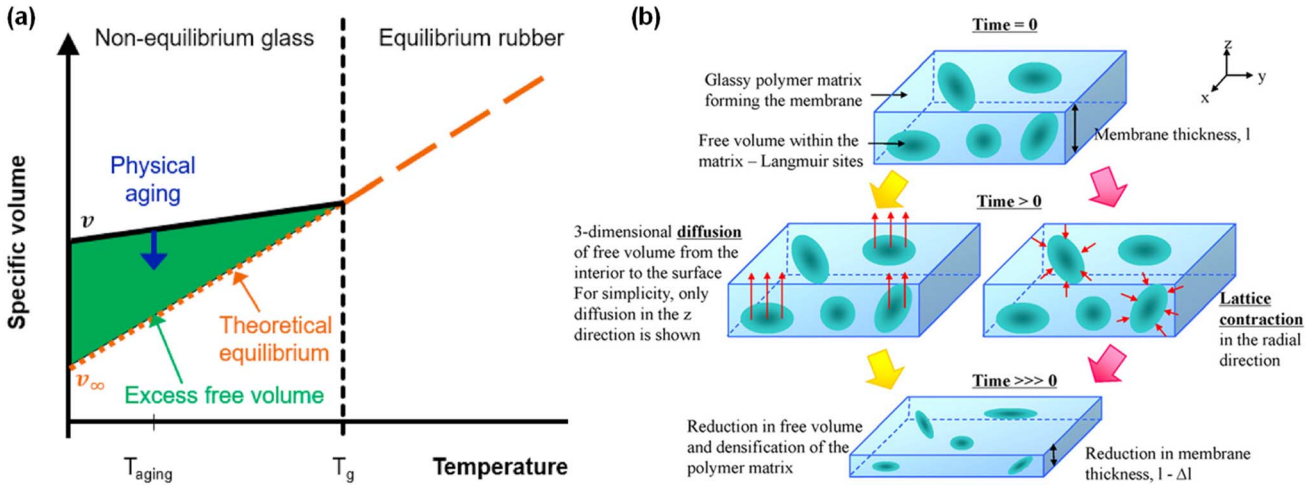

Fig. 15 (a) Specific volume *vs.* temperature for an amorphous polymer. The extrapolated equilibrium specific volume (dashed line) above T_g diverges from the non-equilibrium state (solid line) below T_g, where excess free volume (green area) becomes kinetically trapped. Physical aging (represented by the dark blue arrow) indicates the slow relaxation toward equilibrium. Reprinted with permission from ref. 180, Copyright 2020, Elsevier. (b) Schematic of free volume diffusion and lattice contraction during aging. Reprinted with permission from ref. 155, copyright 2009, Elsevier.

paths that delay free-volume collapse.[194,195] Sutrisna *et al.*[196] stabilized poly(trimethylsilyl)-1-propyne] (PTMSP) gutter layers using ZIF-8/Pebax-1657 composite coatings. Hydrogen bonding between ZIF-8 ligands and polyamide chains enhanced chain rigidity, while interpenetration of Pebax into PTMSP reduced segmental mobility. The composite membrane maintained stable CO_2 permeance (220 ∼ 350 GPU) over 15 days at 2 bar, contrasting with bare PTMSP layers, which lost >22% permeance.

Notably, physical aging also impacts CMS HFMs, where the microporous structure undergoes rearrangement over time after pyrolysis.[197] This structural evolution reduces pore accessibility and constricts critical diffusion pathways, leading to substantial declines in gas permeance. Hybridization and surface engineering effectively address this. Shin *et al.*[198] incorporated ladder-structured poly(phenyl-*co*-pyridylethyl)silsesquioxane (LPPyr64) into a 6FDA-DAM : DABA (3 : 2) polyimide before pyrolysis. The rigid siloxane framework preserved the porous microstructure during pyrolysis, yielding CMS fibers with a CO_2 permeance of 956 GPU, a 546% increase over precursor fibers (148 GPU). However, untreated CMS PI-LPSQ20 fibers exhibited rapid aging, with CO_2 permeance dropping from 956 to 406.9 GPU within 24 hours post-pyrolysis. PDMS-coated CMS PI-LPSQ20 membranes retained a CO_2 permeance of 354 GPU and CO_2/CH_4 selectivity of 56 after 72 days, with no plasticization observed at 13.2 bar CO_2 partial pressure. Kamath *et al.*[199] eliminated aging in 6FDA-DETDA : DABA derived CMSs by esterifying DABA to DABE and pretreating it with 10% vinyltrimethoxysilane (VTMS). This suppressed residual stress-driven rearrangements, stabilizing CO_2 permeance > 1000 GPU for 7 days with a CO_2/CH_4 selectivity of 25 and 780 GPU (selectivity: 48) after 72 days under 21 bar (50 mol% CO_2/CH_4). Synergistic approaches-combining rigid frameworks (LPSQs and MOFs) with polymer backbone engineering and protective coatings (*e.g.*, PDMS)-demonstrate exceptional aging resistance in both polymeric and CMS HFMs.

5.3 Collapse of the nanoporous transition layer

Nanoporous transition layer collapse refers to the densification or structural deformation of the intermediate porous layer between the dense selective skin and the macroporous support in asymmetric HFMs. This phenomenon arises from capillary forces during solvent removal or thermal stresses during high-temperature processing, leading to reduced pore connectivity, thickened skin layers, and diminished gas permeance.[118,200] For instance, in the dry/wet phase inversion process, residual solvents with high surface tension (*e.g.*, water) generate significant capillary forces during drying, tightening the pore structure and increasing substructure resistance. Koros *et al.*[118] demonstrated that Matrimid® 5218 HFMs dried directly from water exhibited a skin layer thickness of 1880 nm with a He permeance of only 12.8 GPU. In contrast, solvent-exchanged fibers (using low-surface-tension fluids like hexane) retained a thinner 730 Å skin layer and achieved a He permeance of 243.5 GPU, with minimal transition layer collapse. Optimal performance (high selectivity and permeance) was achieved by solvent exchange in methanol followed by hexane prior to drying, highlighting the critical role of solvent selection in membrane morphology and performance.

For CMS HFMs, sub-1 μm skin layers are highly susceptible to transition layer collapse. During pyrolysis, precursor hollow fiber substrates often collapse, resulting in CMS membranes with thick skin layers (15–50 μm).[201] Pre-treating precursors with silane (*e.g.*, vinyltrimethoxysilane, VTMS) prior to pyrolysis mitigates substrate collapse, reducing skin thickness to ∼3–6 μm, though still thicker than precursor fibers (Fig. 16b and c).[200] To achieve ultrathin skins (<1 μm), Zhang *et al.*[202] developed dual-layer HFMs combined with silane treatment and *in situ* hybridization (Fig. 16a). After hybridization, dual layer ULT CMS-MA1 membranes with a 1 μm skin layer achieved a CO_2/CH_4 separation factor of 7.9 ∼ 36.7 and CO_2 permeance of ∼1177 GPU, demonstrating effective defect repair. Further

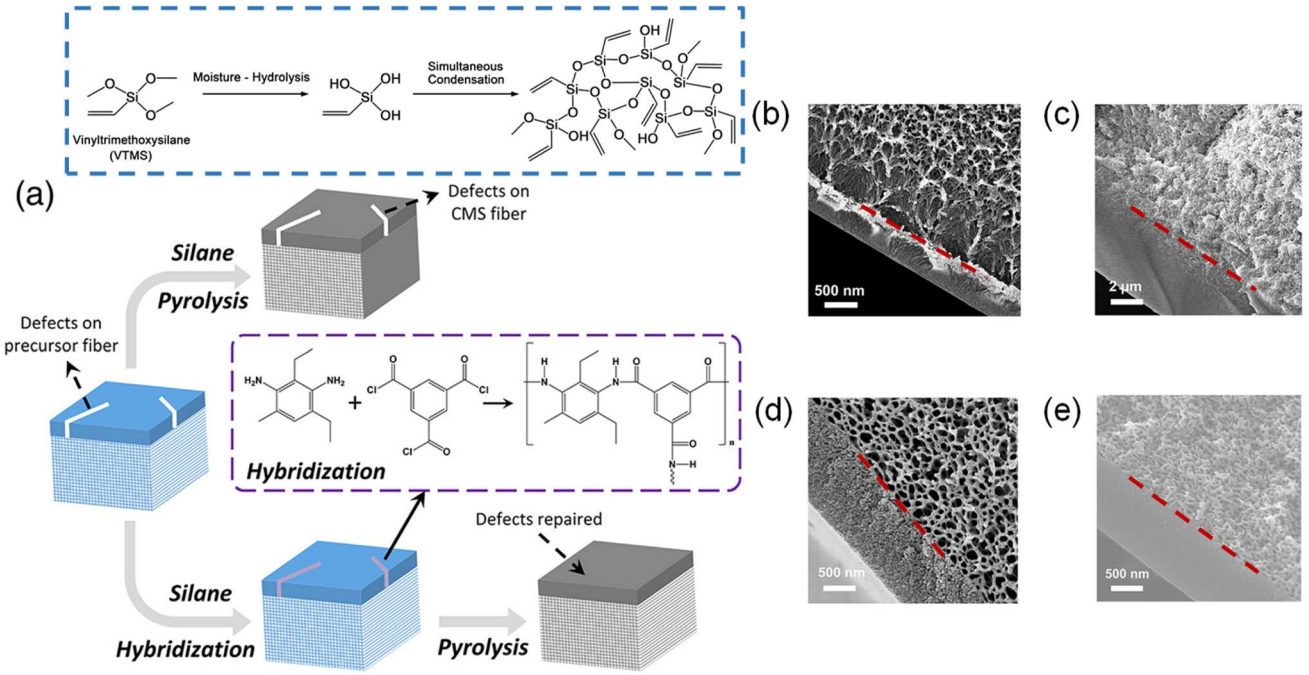

Fig. 16 (a) Schematic of CMS HFM defect repair substrate collapse suppression *via* silane treatment and *in situ* hybridization. (b and c) SEM images of monolithic Matrimid® precursor HF and derived CMS HF with silane treatment (6 μm skin). (d) and (e) SEM images of dual-layer Matrimid®/Matrimid® precursor HF with silane and hybridization treatments, yielding ultrathin (1 μm skin) CMS HF (ULT CMS MA1). Reprinted with permission from ref. 200, Copyright 2019, John Wiley and Sons.

optimization reduced the skin layer to 0.5 μm (Fig. 16d and e), yielding a CO_2 permeance of 1452 GPU and CO_2/CH_4 separation factor of ~18 under an equimolar CO_2/CH_4 feed at 100 PSIA and 35 °C. Emerging strategies such as hierarchical pore structuring, selective silica deposition *via* silane optimization, and hybrid precursor designs are critical for scaling these innovations to industrial applications.

Integrated stabilization strategies empower polymeric hollow fiber membranes to successfully overcome the aforementioned tripartite challenges. Specifically, covalent crosslinking reinforces polymeric networks through three-dimensional bonding, effectively immobilizing polymer chains to suppress swelling-induced plasticization under CO_2 partial pressures exceeding 500 PSIA. Concurrently, nanoconfined architectures incorporating porous fillers mitigate physical aging by sterically stabilizing interconnected free-volume elements, reducing permeance decay through restricted chain segment relaxation. Complementarily, transition-layer integrity is preserved *via* optimized solvent-exchange sequences and silane-based interfacial modifications, enabling ultrathin selective skins (<1 μm) with sustained helium permeance. Strategic implementation necessitates balancing chemical resilience against aggressive feed stream, scalable manufacturing viability, and validated operational stability.

6 Conclusion and outlook

This review resolves two fundamental challenges in polymeric hollow fiber membrane technology for sustainable natural gas valorization. First, hierarchical engineering of asymmetric and composite configurations enables precise transport pathway control, achieving efficient helium recovery from sub-0.3% sources and acid gas removal in complex hydrocarbon streams. Second, molecular confinement strategies utilizing covalent stabilization and nanoscale hybridization mitigate aging and plasticization under demanding conditions. Moving forward, three interconnected frontiers are anticipated to shape next-generation HFMs: computational discovery integrating multiscale modeling with machine learning designs advanced polymers possessing adaptive free volume architectures that overcome traditional selectivity-permeance tradeoffs; circular manufacturing adopting enzymatic monomer regeneration and solvent-free processing reduces environmental footprints while enhancing scalability; hybrid membrane systems combining thermally rearranged polymers with carbon molecular sieve supports enable integrated gas refineries capable of simultaneous carbon capture, methane purification, and helium extraction from lean sources. Realizing this vision requires convergent innovations across computational science, synthetic biology, and modular process engineering to position hollow fiber membranes as intelligent platforms for decarbonized energy infrastructure.

Conflicts of interest

There are no conflicts to declare.

Data availability

No new primary data were generated for this review. For further details, readers are directed to the corresponding references or may contact the authors for specific inquiries.

The data supporting this review article are derived from published studies cited throughout the manuscript. All referenced datasets and experimental results are available in the original publications, as indicated in the reference list.

Supplementary information is available. See DOI: https://doi.org/10.1039/d5ta04814a.

Acknowledgements

The authors would like to extend their sincere gratitude for the financial support received from the Shanxi-Zheda Institute of Advanced Materials and Chemical Engineering (2022SZ-TD014), the Project of Stable Support for Youth Team in Basic Research Field of the Chinese Academy of Sciences (No. YSBR-017), and the National Natural Science Foundation of China (No. 22478396 and 22090063).

References

1 V. Martin-Gil, M. Z. Ahmad, R. Castro-Muñoz and V. Fila, *Sep. Purif. Rev.*, 2018, **48**, 298–324.
2 J. B. Powell, *Catal. Today*, 2020, **356**, 27–36.
3 KPMG International entities, *Statistical Review of World Energy*, Energy Institute, London, 73rd edn, 2024.
4 X. Chen, G. Liu and W. Jin, *Green Energy Environ.*, 2021, **6**, 176–192.
5 Y. Liu, Z. Liu, B. E. Kraftschik, V. P. Babu, N. Bhuwania, D. Chinn and W. J. Koros, *J. Membr. Sci.*, 2021, **632**, 119361.
6 C. J. Berganza and J. H. Zhang, *Med. Gas Res.*, 2013, **3**, 18.
7 A. Cho, *Science*, 2009, **326**, 778–779.
8 W. P. Halperin, *Nat. Phys.*, 2014, **10**, 467–470.
9 M. Mahesh and P. B. Barker, *J. Am. Coll. Radiol.*, 2016, **13**, 1536–1537.
10 R. W. Baker and K. Lokhandwala, *Ind. Eng. Chem. Res.*, 2008, **47**, 2109–2121.
11 S. Cavenati, C. A. Grande and A. E. Rodrigues, *Chem. Eng. Sci.*, 2006, **61**, 3893–3906.
12 M. Rezakazemi, I. Heydari and Z. Zhang, *J. CO_2 Util.*, 2017, **18**, 362–369.
13 R. W. Baker and B. T. Low, *Macromolecules*, 2014, **47**, 6999–7013.
14 P. Zheng, W. Xie, Z. Cai, Y. Jiao, Y. Sun, T. Han, X. Ma, N. Li and S. Luo, *J. Membr. Sci.*, 2023, **672**, 121425.
15 A. Imtiaz, M. H. D. Othman, A. Jilani, I. U. Khan, R. Kamaludin, J. Iqbal and A. G. Al-Sehemi, *Membranes*, 2022, **12**, 646.
16 R. W. Baker, *Ind. Eng. Chem. Res.*, 2002, **41**, 1393–1411.
17 G. Li, W. Kujawski, R. Válek and S. Koter, *Int. J. Greenhouse Gas Control*, 2021, **104**, 103195.
18 X. Y. Chen, S. Kaliaguine and D. Rodrigue, *Sep. Purif. Rev.*, 2017, **47**, 66–87.
19 C. F. Wan, T. Yang, G. G. Lipscomb, D. J. Stookey and T.-S. Chung, *J. Membr. Sci.*, 2017, **538**, 96–107.
20 Y. Huang, C. Xiao, Q. Huang, H. Liu and J. Zhao, *Chem. Eng. J.*, 2021, **403**, 126295.
21 C. A. Scholes, G. W. Stevens and S. E. Kentish, *Fuel*, 2012, **96**, 15–28.
22 K. Y. Wang, M. Weber and T.-S. Chung, *J. Mater. Chem. A*, 2022, **10**, 8687–8718.
23 S. Luo, T. Han, C. Wang, Y. Sun, H. Zhang, R. Guo and S. Zhang, *Ind. Chem. Mater.*, 2023, **1**, 376–387.
24 N. Peng, N. Widjojo, P. Sukitpaneenit, M. M. Teoh, G. G. Lipscomb, T.-S. Chung and J.-Y. Lai, *Prog. Polym. Sci.*, 2012, **37**, 1401–1424.
25 I. Ullah Khan, M. H. D. Othman, A. F. Ismail, T. Matsuura, H. Hashim, N. A. H. M. Nordin, M. A. Rahman, J. Jaafar and A. Jilani, *J. Nat. Gas Sci. Eng.*, 2018, **52**, 215–234.
26 H. S. Lau and W. F. Yong, *J. Mater. Chem. A*, 2021, **9**, 26454–26497.
27 R. A. Roslan, W. J. Lau, A. F. Ismail and S. Kartohardjono, *J. Mater. Sci.*, 2024, **59**, 10083–10118.
28 S. Shah, J. Liu, S. Ng, S. Luo, R. Guo, C. Cheng and H. Lin, *J. Polym. Sci., Part B: Polym. Phys.*, 2016, **54**, 1924–1934.
29 Y. Jia, K. Wong, C. Liang, J. Wu, T. Chung and S. Zhang, *Prog. Mater. Sci.*, 2024, **146**, 101324.
30 C. Arregoitia-Sarabia, D. Gonzalez-Revuelta, M. Fallanza, A. Ortiz and D. Gorri, *Membranes*, 2022, **12**, 1007.
31 L. M. Robeson, *J. Membr. Sci.*, 2008, **320**, 390–400.
32 E. P. Favvas, F. K. Katsaros, S. K. Papageorgiou, A. A. Sapalidis and A. C. Mitropoulos, *React. Funct. Polym.*, 2017, **120**, 104–130.
33 J. G. Wijmans and R. W. Baker, *J. Membr. Sci.*, 1995, **107**, 1–21.
34 N. Du, H. B. Park, M. M. Dal-Cin and M. D. Guiver, *Energy Environ. Sci.*, 2012, **5**, 7306–7322.
35 H. B. Park, J. Kamcev, L. M. Robeson, M. Elimelech and B. D. Freeman, *Science*, 2017, **356**, eaab0530.
36 M. Wang, J. Zhao, X. Wang, A. Liu and K. K. Gleason, *J. Mater. Chem. A*, 2017, **5**, 8860–8886.
37 S. Zhang, *Green Energy Environ.*, 2023, **8**, 1229–1231.
38 H. Lin and M. Yavari, *J. Membr. Sci.*, 2015, **475**, 101–109.
39 Y. Seo, S. U. Hong and B. S. Lee, *Angew. Chem., Int. Ed.*, 2003, **42**, 1145–1149.
40 A. X. Wu, J. A. Drayton and Z. P. Smith, *AIChE J.*, 2019, **65**, e16700.
41 A. W. Thornton, T. Hilder, A. J. Hill and J. M. Hill, *J. Membr. Sci.*, 2009, **336**, 101–108.
42 T. A. Centeno and A. B. Fuertes, *J. Membr. Sci.*, 1999, **160**, 201–211.
43 B. Petrovic, M. Gorbounov and S. M. Soltani, *Microporous Mesoporous Mater.*, 2021, **312**, 110751.
44 E. R. Gilliland, R. F. Baddour, G. P. Perkinson and K. J. Sladek, *Ind. Eng. Chem. Fundam.*, 1974, **13**, 95–100.
45 P. Pandey and R. Chauhan, *Prog. Polym. Sci.*, 2001, **26**, 853–893.
46 S. Higgins, W. DeSisto and D. Ruthven, *Microporous Mesoporous Mater.*, 2009, **117**, 268–277.
47 L. Jiang, T.-S. Chung, D. F. Li, C. Cao and S. Kulprathipanja, *J. Membr. Sci.*, 2004, **240**, 91–103.
48 M. Liu, M. D. Nothling, P. A. Webley, Q. Fu and G. G. Qiao, *Acc. Chem. Res.*, 2019, **52**, 1905–1914.
49 G. J. Dahe, R. P. Singh, K. W. Dudeck, D. Yang and K. A. Berchtold, *J. Membr. Sci.*, 2019, **577**, 91–103.

50 Y. D. Kim, J. Y. Kim, H. K. Lee and S. C. Kim, *J. Membr. Sci.*, 2001, **190**, 69–77.
51 L. Liu, E. S. Sanders, J. R. Johnson, O. Karvan, S. Kulkarni, D. J. Hasse and W. J. Koros, *J. Membr. Sci.*, 2013, **446**, 433–439.
52 Y. Zhang, Y. Chen, X. Hu, B. Cheng and H. Liu, *Macromol. Mater. Eng.*, 2017, **302**, 1700282.
53 D. Wang, K. Li and W. K. Teo, *J. Membr. Sci.*, 2002, **208**, 419–426.
54 H. Hasbullah, S. Kumbharkar, A. F. Ismail and K. Li, *J. Membr. Sci.*, 2011, **366**, 116–124.
55 W. Qiu, L. Liu and W. J. Koros, *J. Membr. Sci.*, 2017, **529**, 150–158.
56 D. Wang, W. K. Teo and K. Li, *J. Membr. Sci.*, 2002, **204**, 247–256.
57 Z. Li, X. Liu, Y. Sun, L. Gong, C. Liao and S. Luo, *Polymer*, 2025, **323**, 128164.
58 L. Liu, Q. Wu, S. Wang, W. Lai, P. Zheng, C. Wang, X. Wei and S. Luo, *Ind. Eng. Chem. Res.*, 2022, **62**, 708–716.
59 M. R. Kosuri and W. J. Koros, *J. Membr. Sci.*, 2008, **320**, 65–72.
60 W. F. Yong, F. Y. Li, Y. C. Xiao, T. S. Chung and Y. W. Tong, *J. Membr. Sci.*, 2013, **443**, 156–169.
61 M. L. Jue, V. Breedveld and R. P. Lively, *J. Membr. Sci.*, 2017, **530**, 33–41.
62 T. Hu, G. Dong, H. Li and V. Chen, *J. Membr. Sci.*, 2014, **468**, 107–117.
63 X. Ding, Y. Cao, H. Zhao, L. Wang and Q. Yuan, *J. Membr. Sci.*, 2008, **323**, 352–361.
64 T. He, M. H. V. Mulder, H. Strathmann and M. Wessling, *J. Membr. Sci.*, 2002, **207**, 143–156.
65 F. Y. Li, Y. Li, T.-S. Chung, H. Chen, Y. C. Jean and S. Kawi, *J. Membr. Sci.*, 2011, **378**, 541–550.
66 L. Jiang, *J. Membr. Sci.*, 2004, **240**, 91–103.
67 A. Raza, M. Askari, C. Z. Liang, N. Peng, S. Farrukh, A. Hussain and T.-S. Chung, *J. Membr. Sci.*, 2021, **625**, 119124.
68 Y. Li and T.-S. Chung, *J. Membr. Sci.*, 2010, **350**, 226–231.
69 Y. Liu, T.-S. Chung, R. Wang, D. F. Li and M. L. Chng, *Ind. Eng. Chem. Res.*, 2003, **42**, 1190–1195.
70 C. Ma and W. J. Koros, *Ind. Eng. Chem. Res.*, 2013, **52**, 10495–10505.
71 W. Xie, Y. Jiao, Z. Cai, H. Liu, L. Gong, W. Lai, L. Shan and S. Luo, *Sep. Purif. Technol.*, 2022, **282**, 120091.
72 A. U. Khan, O. Samuel, M. H. D. Othman, M. Younas, R. Kamaludin, Z. I. Khan, M. F. A. Al-Ogaili, N. Yoshida, T. A. Kurniawan, M. H. Puteh, F. Kadirkhan, M. O. Aijaz and M. R. Karim, *J. Environ. Chem. Eng.*, 2025, **13**, 114913.
73 G. Li, W. Kujawski, R. Válek and S. Koter, *Int. J. Greenhouse Gas Control*, 2021, **104**, 103195.
74 S. Li, Y. Liu, D. A. Wong and J. Yang, *Polymers*, 2021, **13**, 2539.
75 L. Liu, A. Chakma and X. Feng, *Ind. Eng. Chem. Res.*, 2005, **44**, 6874–6882.
76 W. Lai, L. Liu, J. Bai, L. Xiao, Y. Jiao, Y. Yang, L. Shan and S. Luo, *Chem. Eng. J.*, 2023, **460**, 141708.
77 K. C. Khulbe and T. Matsuura, *Polymers*, 2018, **10**, 1051.
78 Q. Wu, Y. Jiao, L. Liu, Y. Sun, T. Han, Y. Peng, W. Yang, S. Luo and S. Zhang, *Chem. Eng. J.*, 2023, **461**, 141976.
79 P. Li, H. Z. Chen and T.-S. Chung, *J. Membr. Sci.*, 2013, **434**, 18–25.
80 Z. Dai, J. Deng, Q. Yu, R. M. L. Helberg, S. Janakiram, L. Ansaloni and L. Deng, *ACS Appl. Mater. Interfaces*, 2019, **11**, 10874–10882.
81 G. Chowdhury, S. Deng, T. Matsuura and B. Laverty, *J. Appl. Polym. Sci.*, 2001, **79**, 275–282.
82 J.-J. Qin and T.-S. Chung, *Desalination*, 2006, **192**, 112–116.
83 H. B. Li, W. Y. Shi, J. C. Li and Y. F. Zhang, *Fibers Polym.*, 2014, **15**, 2553–2563.
84 G. V. Theodorakopoulos, D. S. Karousos, K. G. Mansouris, A. A. Sapalidis, E. P. Kouvelos and E. P. Favvas, *Int. J. Greenhouse Gas Control*, 2022, **114**, 103588.
85 S. V. Gutiérrez-Hernández, F. Pardo, A. B. Foster, P. M. Budd, G. Zarca and A. Urtiaga, *Sep. Purif. Technol.*, 2025, **363**, 132254.
86 W. Lai, L. Liu, J. Bai, L. Xiao, Y. Jiao, Y. Yang, L. Shan and S. Luo, *Chem. Eng. J.*, 2023, **460**, 141708.
87 E.-S. Jo, X. An, P. G. Ingole, W.-K. Choi, Y.-S. Park and H.-K. Lee, *Chin. J. Chem. Eng.*, 2017, **25**, 278–287.
88 S.-H. Choi, M. M. B. Sultan, A. A. Alsuwailem and S. M. Zuabi, *Sep. Purif. Technol.*, 2019, **222**, 152–161.
89 L. Tao, J. He, T. Arbaugh, J. R. McCutcheon and Y. Li, *J. Membr. Sci.*, 2023, **665**, 121131.
90 J. Xu, A. Suleiman, G. Liu, R. Zhang, M. Jiang, R. Guo and T. Luo, *Chem. Phys. Rev.*, 2024, **5**, 041311.
91 F. Mokhtari, A. Samadi, A. O. Rashed, X. Li, J. M. Razal, L. Kong, R. J. Varley and S. Zhao, *Prog. Mater. Sci.*, 2025, **148**, 101376.
92 I. V. Farr, T. E. Glass, Q. Ji and J. E. McGrath, *High Perform. Polym.*, 2016, **9**, 345–352.
93 D. F. Sanders, Z. P. Smith, R. Guo, L. M. Robeson, J. E. McGrath, D. R. Paul and B. D. Freeman, *Polymer*, 2013, **54**, 4729–4761.
94 J. R. Weidman, S. Luo, J. M. Breier, P. Buckley, P. Gao and R. Guo, *Polymer*, 2017, **126**, 314–323.
95 Z. Mao, X. Jie, Y. Cao, L. Wang, M. Li and Q. Yuan, *Sep. Purif. Technol.*, 2011, **77**, 179–184.
96 Z. Jahan, M. B. K. Niazi, M.-B. Hägg and Ø. W. Gregersen, *J. Membr. Sci.*, 2018, **554**, 275–281.
97 D. Nikolaeva, I. Azcune, M. Tanczyk, K. Warmuzinski, M. Jaschik, M. Sandru, P. I. Dahl, A. Genua, S. Loïs, E. Sheridan, A. Fuoco and I. F. J. Vankelecom, *J. Membr. Sci.*, 2018, **564**, 552–561.
98 P. Tanvidkar, B. Nayak and B. V. R. Kuncharam, *J. Polym. Environ.*, 2023, **31**, 3404–3417.
99 E. Sada, H. Kumazawa, J.-S. Wang and M. Kolzuml, *J. Appl. Polym. Sci.*, 1992, **45**, 2181–2186.
100 M. M. Rajpure, R. B. Mujmule, U. Kim and H. Kim, *Int. J. Hydrogen Energy*, 2024, **50**, 615–628.
101 Y.-W. Jeon and M.-S. Shin, *Energy Procedia*, 2017, **136**, 219–224.
102 N. Sunder, Y.-Y. Fong, M. A. Bustam and W.-J. Lau, *Separations*, 2023, **10**, 41–54.

103 S.-H. Pak, Y.-W. Jeon, M.-S. Shin and H. C. Koh, *Environ. Eng. Sci.*, 2016, **33**, 17–24.
104 M. Mubashir, Y. F. Yeong, K. K. Lau and T. L. Chew, *Polym. Test.*, 2019, **73**, 1–11.
105 M. Mubashir, Y. F. Yeong, T. L. Chew and K. K. Lau, *Sep. Purif. Technol.*, 2019, **215**, 32–43.
106 M. Mubashir, Y. Yin fong, C. T. Leng, L. K. Keong and N. Jusoh, *Polym. Test.*, 2020, **81**, 106223.
107 A. F. Ismail and W. Lorna, *Sep. Purif. Technol.*, 2003, **30**, 37–46.
108 A. J. Erb and D. R. Paul, *J. Membr. Sci.*, 1981, **8**, 11–22.
109 A. Naderi, W. F. Yong, Y. Xiao, T.-S. Chung, M. Weber and C. Maletzko, *Polymer*, 2018, **135**, 76–84.
110 R. Guo and J. E. McGrath, *Polym. Sci.*, 2012, 377–430, DOI: 10.1016/b978-0-444-53349-4.00153-9.
111 C. L. Aitken, W. J. Koros and D. R. Paul, *Macromolecules*, 2002, **25**, 3651–3658.
112 W. F. Yong, T.-S. Chung, M. Weber and C. Maletzko, *J. Membr. Sci.*, 2018, **552**, 305–314.
113 X. Liu, B. Cao and P. Li, *Ind. Eng. Chem. Res.*, 2017, **57**, 329–338.
114 R. A. Roslan, W. J. Lau, A. K. Zulhairun, P. S. Goh and A. F. Ismail, *J. Polym. Res.*, 2020, **27**, 119–133.
115 I. U. Khan, M. H. D. Othman, A. Jilani, A. F. Ismail, H. Hashim, J. Jaafar, A. K. Zulhairun, M. A. Rahman and G. U. Rehman, *Polym. Test.*, 2020, **84**, 106415.
116 B. Sasikumar, S. Bisht, G. Arthanareeswaran, A. F. Ismail and M. H. D. Othman, *Sep. Purif. Technol.*, 2021, **264**, 118471.
117 A. Sharif, H. Koolivand, G. Khanbabaie, M. Hemmati, J. Aalaie, M. R. Kashani and A. Gheshlaghi, *J. Polym. Res.*, 2012, **19**, 9916.
118 D. T. Clausi and W. J. Koros, *J. Membr. Sci.*, 2000, **167**, 79–89.
119 Y. Zhuang, J. G. Seong and Y. M. Lee, *Prog. Polym. Sci.*, 2019, **92**, 35–88.
120 I. V. Farr, D. Kratzner, T. E. Glass, D. Dunson, Q. Ji and J. E. McGrath, *J. Polym. Sci., Part A: Polym. Chem.*, 2000, **38**, 2840–2854.
121 X. Chen, S. Kaliaguine and D. Rodrigue, *J. Membr. Sep. Technol.*, 2017, **6**, 1–15.
122 P. Tin, *J. Membr. Sci.*, 2003, **225**, 77–90.
123 C. Cao, R. Wang, T. S. Chung and Y. Liu, *J. Membr. Sci.*, 2002, **209**, 309–319.
124 S. V. Gutiérrez-Hernández, S. Rico-Martínez, F. Pardo, C. Álvarez, J. A. Miguel, G. Zarca and A. Urtiaga, *J. Membr. Sci.*, 2024, **698**, 122617.
125 H. Hachisuka, T. Ohara and K. Ikeda, *J. Membr. Sci.*, 1996, **116**, 265–272.
126 J.-J. Qin, T.-S. Chung, C. Cao and R. H. Vora, *J. Membr. Sci.*, 2005, **250**, 95–103.
127 L. Xu, C. Zhang, M. Rungta, W. Qiu, J. Liu and W. J. Koros, *J. Membr. Sci.*, 2014, **459**, 223–232.
128 J. Lee, J. S. Kim, J. F. Kim, H. J. Jo, H. Park, J. G. Seong and Y. M. Lee, *J. Membr. Sci.*, 2019, **573**, 393–402.
129 S. Kim and Y. M. Lee, *J. Nanopart. Res.*, 2012, **14**, 949–960.
130 K. T. Woo, J. Lee, G. Dong, J. S. Kim, Y. S. Do, W.-S. Hung, K.-R. Lee, G. Barbieri, E. Drioli and Y. M. Lee, *J. Membr. Sci.*, 2015, **490**, 129–138.
131 K. T. Woo, J. Lee, G. Dong, J. S. Kim, Y. S. Do, H. J. Jo and Y. M. Lee, *J. Membr. Sci.*, 2016, **498**, 125–134.
132 K. T. Woo, G. Dong, J. Lee, J. S. Kim, Y. S. Do, W. H. Lee, H. S. Lee and Y. M. Lee, *J. Membr. Sci.*, 2016, **510**, 472–480.
133 J. Lee, J. S. Kim, S.-y. Moon, C. Y. Park, J. F. Kim and Y. M. Lee, *J. Membr. Sci.*, 2020, **595**, 117535.
134 S. Kim, S. H. Han and Y. M. Lee, *J. Membr. Sci.*, 2012, **403–404**, 169–178.
135 S. Fan, C. Niu, W. Duan, Z. Sun, B. Chen, Z. Ren, J. Wang, G. Tang, G. Zhao, Y. Liu and P. Li, *J. Membr. Sci.*, 2025, **713**, 123305.
136 Y. Jiao, Q. Wu, W. Xu, W. Lai, L. Xiao, X. Mei, H. Zhang and S. Luo, *Sep. Purif. Technol.*, 2023, **315**, 123691.
137 C. Zhang, K. Zhang, Y. Cao and W. J. Koros, *Ind. Eng. Chem. Res.*, 2018, **57**, 16051–16058.
138 Y. Ma, M. L. Jue, F. Zhang, R. Mathias, H. Y. Jang and R. P. Lively, *Angew. Chem., Int. Ed.*, 2019, **58**, 13259–13265.
139 O. Karvan, J. R. Johnson, P. J. Williams and W. J. Koros, *Chem. Eng. Technol.*, 2013, **36**, 53–61.
140 G. Liu, Y. Labreche, N. Li, Y. Liu, C. Zhang, S. J. Miller, V. P. Babu, N. Bhuwania and W. J. Koros, *AIChE J.*, 2019, **65**, 1269–1280.
141 Y. Ma, M. L. Jue, F. Zhang, R. Mathias, H. Y. Jang and R. P. Lively, *Angew. Chem., Int. Ed.*, 2019, **58**, 13259–13265.
142 D. Q. Vu and W. J. Koros, *Ind. Eng. Chem. Res.*, 2002, **41**, 367–380.
143 C. Zhang and W. J. Koros, *Adv. Mater.*, 2017, **29**, 1701631.
144 M. G. Kamath, A. K. Itta, S. S. Hays, O. Sanyal, Z. Liu and W. J. Koros, *Ind. Eng. Chem. Res.*, 2020, **59**, 13755–13761.
145 Q. Wu, L. Liu, Y. Jiao, Z. Y. Li, J. Bai, X. H. Ma, S. J. Luo and S. J. Zhang, *Angew. Chem., Int. Ed.*, 2024, **63**, e202400688.
146 C. Zhang, G. B. Wenz, P. J. Williams, J. M. Mayne, G. Liu and W. J. Koros, *Ind. Eng. Chem. Res.*, 2017, **56**, 10482–10490.
147 L. Lei, A. Lindbråthen, X. Zhang, E. P. Favvas, M. Sandru, M. Hillestad and X. He, *J. Membr. Sci.*, 2020, **614**, 118529.
148 Y. Cao, K. Zhang, O. Sanyal and W. J. Koros, *Angew. Chem., Int. Ed.*, 2019, **58**, 12149–12153.
149 Y. Cao, Z. Liu, W. Qiu and W. J. Koros, *Angew. Chem., Int. Ed.*, 2023, **62**, e202303915.
150 K. Tanaka, A. Taguchi, J. Hao, H. Kita and K. Okamoto, *J. Membr. Sci.*, 1996, **121**, 197–207.
151 K. Okamoto, K. Noborio, H. Jianqiang, K. Tanaka and H. Kita, *J. Membr. Sci.*, 1997, **134**, 171–179.
152 J. D. Wind, S. M. Sirard, D. R. Paul, P. F. Green, K. P. Johnston and W. J. Koros, *Macromolecules*, 2003, **36**, 6433–6441.
153 K. Mizrahi Rodriguez, S. Lin, A. X. Wu, K. R. Storme, T. Joo, A. F. Grosz, N. Roy, D. Syar, F. M. Benedetti and Z. P. Smith, *Chem. Soc. Rev.*, 2024, **53**, 2435–2529.
154 L. S. White, T. A. Blinka, H. A. Kloczewski and I. f. Wang, *J. Membr. Sci.*, 1995, **103**, 73–82.
155 Y. Xiao, B. T. Low, S. S. Hosseini, T. S. Chung and D. R. Paul, *Prog. Polym. Sci.*, 2009, **34**, 561–580.

156 J. D. Wind, D. R. Paul and W. J. Koros, *J. Membr. Sci.*, 2004, **228**, 227–236.
157 C. Cao, *J. Membr. Sci.*, 2003, **216**, 257–268.
158 C.-C. Chen, W. Qiu, S. J. Miller and W. J. Koros, *J. Membr. Sci.*, 2011, **382**, 212–221.
159 T. Rodenas, I. Luz, G. Prieto, B. Seoane, H. Miro, A. Corma, F. Kapteijn, F. X. Llabrés i Xamena and J. Gascon, *Nat. Mater.*, 2014, **14**, 48–55.
160 J. E. Bachman and J. R. Long, *Energy Environ. Sci.*, 2016, **9**, 2031–2036.
161 A. Bos, I. G. M. Pünt, M. Wessling and H. Strathmann, *J. Membr. Sci.*, 1999, **155**, 67–78.
162 G. Dong, H. Li and V. Chen, *J. Membr. Sci.*, 2011, **369**, 206–220.
163 J. Ren, R. Wang, T.-S. Chung, D. F. Li and Y. Liu, *J. Membr. Sci.*, 2003, **222**, 133–147.
164 W. Qiu, C.-C. Chen, L. Xu, L. Cui, D. R. Paul and W. J. Koros, *Macromolecules*, 2011, **44**, 6046–6056.
165 Y. Liu, Z. Liu, A. Morisato, N. Bhuwania, D. Chinn and W. J. Koros, *J. Membr. Sci.*, 2020, **601**, 117910.
166 H. J. Yu, H. An, J. H. Shin, A. Brunetti and J. S. Lee, *Chem. Eng. J.*, 2023, **473**, 145378.
167 Y. Jiao, Q. Wu, W. Xu, W. Lai, L. Xiao, X. Mei, H. Zhang and S. Luo, *Sep. Purif. Technol.*, 2023, **315**, 123691.
168 Z. Li, T. Han, W. Lai, J. Ma, Y. Zhang, Q. Wu, C. Wang, C. Liao and S. Luo, *J. Membr. Sci.*, 2023, **688**, 122126.
169 C. Wang, Z. Li, J. Bai, H. Liu, X. Wang and S. Luo, *Sep. Purif. Technol.*, 2025, **354**, 129019.
170 D. W. Wallace, J. Williams, C. Staudt-Bickel and W. J. Koros, *Polymer*, 2006, **47**, 1207–1216.
171 V. P. Babu, B. E. Kraftschik and W. J. Koros, *J. Membr. Sci.*, 2018, **558**, 94–105.
172 Z. Li, W. Lai, Y. Sun, T. Han, X. Liu, C. Liao and S. Luo, *J. Membr. Sci.*, 2025, **715**, 123480.
173 G. Liu, N. Li, S. J. Miller, D. Kim, S. Yi, Y. Labreche and W. J. Koros, *Angew. Chem., Int. Ed.*, 2016, **55**, 13754–13758.
174 C. Cao, T.-S. Chung, Y. Liu, R. Wang and K. P. Pramoda, *J. Membr. Sci.*, 2003, **216**, 257–268.
175 J. Ren, R. Wang, T.-S. Chung, D. F. Li and Y. Liu, *J. Membr. Sci.*, 2003, **222**, 133–147.
176 J. D. Wind, C. Staudt-Bickel, D. R. Paul and W. J. Koros, *Ind. Eng. Chem. Res.*, 2002, **41**, 6139–6148.
177 N. Alaslai, B. Ghanem, F. Alghunaimi, E. Litwiller and I. Pinnau, *J. Membr. Sci.*, 2016, **505**, 100–107.
178 T.-S. Chung, J. Ren, R. Wang, D. Li, Y. Liu, K. P. Pramoda, C. Cao and W. W. Loh, *J. Membr. Sci.*, 2003, **214**, 57–69.
179 D. Cangialosi, V. M. Boucher, A. Alegría and J. Colmenero, *Soft Matter*, 2013, **9**, 8619.
180 M. M. Merrick, R. Sujanani and B. D. Freeman, *Polymer*, 2020, **211**, 123176.
181 T.-S. Chung and S. Khean Teoh, *J. Membr. Sci.*, 1999, **152**, 175–188.
182 W.-H. Lin and T.-S. Chung, *J. Membr. Sci.*, 2001, **186**, 183–193.
183 B. W. Rowe, B. D. Freeman and D. R. Paul, *Polymer*, 2009, **50**, 5565–5575.
184 B. W. Rowe, B. D. Freeman and D. R. Paul, *Polymer*, 2010, **51**, 3784–3792.
185 G. Clarizia, F. Tasselli and P. Bernardo, *Polymers*, 2020, **12**, 441.
186 J. Xia, T.-S. Chung and D. R. Paul, *J. Membr. Sci.*, 2014, **450**, 457–468.
187 P. H. Pfromm and W. J. Koros, *Polymer*, 1995, **36**, 2379–2387.
188 C. Ma and W. J. Koros, *J. Membr. Sci.*, 2018, **551**, 214–221.
189 Z.-X. Low, P. M. Budd, N. B. McKeown and D. A. Patterson, *Chem. Rev.*, 2018, **118**, 5871–5911.
190 D. S. Bakhtin, S. E. Sokolov, I. L. Borisov, V. V. Volkov, A. V. Volkov and V. O. Samoilov, *Membranes*, 2023, **13**, 519.
191 Y. Jiao, M. Liu, Q. Wu, P. Zheng, W. Xu, B. Ye, H. Zhang, R. Guo and S. Luo, *J. Membr. Sci.*, 2023, **672**, 121474.
192 Z. Kang, L. Fan and D. Sun, *J. Mater. Chem. A*, 2017, **5**, 10073–10091.
193 C. Ma and W. J. Koros, *J. Membr. Sci.*, 2018, **551**, 214–221.
194 F. Mokhtari, K. A. S. Usman, J. Zhang, R. Komljenovic, Ž. Simon, B. Dharmasiri, A. Rezk, P. C. Sherrell, L. C. Henderson, R. J. Varley and J. M. Razal, *ACS Appl. Mater. Interfaces*, 2025, **17**, 3214–3228.
195 S. M. S. Rana, M. T. Rahman, M. S. Sharma, P. Maharjan, T. Bhatta, H. Cho, C. Park and J. Y. Park, *ACS Appl. Mater. Interfaces*, 2021, **13**, 4955–4967.
196 P. D. Sutrisna, J. Hou, H. Li, Y. Zhang and V. Chen, *J. Membr. Sci.*, 2017, **524**, 266–279.
197 X. He, J. A. Lie, E. Sheridan and M.-B. Hägg, *Ind. Eng. Chem. Res.*, 2011, **50**, 2080–2087.
198 J. H. Shin, H. J. Yu, H. An, A. S. Lee, S. S. Hwang, S. Y. Lee and J. S. Lee, *J. Membr. Sci.*, 2019, **570–571**, 504–512.
199 M. G. Kamath, S. Fu, A. K. Itta, W. Qiu, G. Liu, R. Swaidan and W. J. Koros, *J. Membr. Sci.*, 2018, **546**, 197–205.
200 N. Bhuwania, Y. Labreche, C. S. K. Achoundong, J. Baltazar, S. K. Burgess, S. Karwa, L. Xu, C. L. Henderson, P. J. Williams and W. J. Koros, *Carbon*, 2014, **76**, 417–434.
201 L. Xu, M. Rungta and W. J. Koros, *J. Membr. Sci.*, 2011, **380**, 138–147.
202 C. Zhang, R. Kumar and W. J. Koros, *AIChE J.*, 2019, **65**, e16611.